

1 Metabolic control of adult neural stem cell self-renewal by the mitochondrial 2 protease YME1L

3 Gulzar A. Wani¹, Hans-Georg Sprenger², Kristiano Ndoci¹, Srikanth Chandragiri², Richard
4 James Acton¹, Désirée Schatton¹, Sandra M.V. Kochan¹, Vignesh Sakthivelu¹, Milica Jevtic¹,
5 Jens M. Seeger³, Stefan Müller^{1,4}, Patrick Giavalisco², Elena I. Rugarli^{1,4,5}, Elisa Motori^{1,2},
6 Thomas Langer^{1,2} and Matteo Bergami^{1,4,5,6,*,#}

⁸ ¹Cologne Excellence Cluster on Cellular Stress Responses in Aging-Associated Diseases
⁹ (CECAD), University of Cologne, Joseph-Stelzmann-Str. 26, D-50931 Cologne, Germany.

10 ²Max Planck Institute for Biology of Ageing, Joseph-Stelzmann-Str. 9b, D-50931 Cologne,
11 Germany.

12 ³Institute for Medical Microbiology, Immunology and Hygiene (IMMIH), CECAD Research
13 Center and University Hospital Cologne, Joseph-Stelzmann-Str. 26, D-50931 Cologne,
14 Germany.

15 ⁴Center for Molecular Medicine, Robert-Koch-Str. 21, 50931 Cologne, Germany

16 ⁵Institute of Genetics, Zülpicher Str. 47a, D-50674, University of Cologne, Germany

17 ⁶University of Cologne, Faculty of Medicine and University Hospital Cologne, Kerpener Str. 62,
18 D-50937 Cologne, Germany.

19 *Correspondence to: Matteo Bergami

20 CECAD-University Hospital of Cologne, Germany

21 Email: matteo.bergami@uk-koeln.de

22 Phone: +49 (0)221 478 84250

23 # Lead contact: Matteo Bergami

24 CECAD-University Hospital of Cologne, Germany

25 Email: matteo.bergami@uk-koeln.de

26 Phone: +49 (0)221 478 84250

30 **Abstract**

31 The transition between quiescence and activation in neural stem and progenitor cells (NSPCs) is
32 coupled to reversible changes in energy metabolism with key implications for life-long NSPC self-
33 renewal and neurogenesis. How this metabolic plasticity is ensured between NSPC activity states
34 is unclear. We found that a state-dependent rewiring of the mitochondrial proteome by the
35 peptidase YME1L is required to preserve NSPC self-renewal in the adult brain. YME1L-mediated
36 proteome rewiring regulates the rate of fatty acid oxidation (FAO) for replenishing Krebs cycle
37 intermediates and dNTP precursors, which are required to sustain NSPC amplification. *Yme1l*
38 deletion irreversibly shifts the metabolic profile of NSPCs away from a FAO-dependent state
39 resulting in defective self-renewal, premature differentiation and NSPC pool depletion. Our results
40 disclose an important role for YME1L in coordinating the switch between metabolic states of
41 NSPCs and suggest that NSPC fate is regulated by compartmentalized changes in protein network
42 dynamics.

43

44

45

46

47

48

49

50

51

52

53

54

55

56

57

58

59

60

61 **Introduction**

62 Neural stem and progenitor cells (NSPCs) are retained exclusively in few restricted regions of the
63 adult mammalian brain, where they generate new neurons that contribute to specific forms of brain
64 plasticity life-long (Goncalves et al., 2016). Maintenance of this long-lived pool of NSPCs into
65 adulthood is guaranteed by their capability to reversibly switch between proliferative and quiescent
66 states, which confers protection from damage but also prevents irreversible NSPC pool depletion
67 (Navarro Negredo et al., 2020).

68 The activity state of adult NSPCs is regulated on multiple levels. Cell-autonomously,
69 quality control mechanisms ensuring protein homeostasis like the proteasome and lysosomal-
70 autophagic systems are regulated differentially between quiescent and activated states, and can be
71 manipulated to control NSPC fate (Leeman et al., 2018; Morrow et al., 2020; Schaffner et al.,
72 2018). Likewise, specific metabolic programs including changes in lipid metabolism, reactive
73 oxygen species (ROS) signalling, redox state, glutaminolysis and mitochondrial oxidative
74 phosphorylation (OXPHOS) mark the switch between cellular stages along the embryonic and
75 adult NSPC lineage (Adusumilli et al., 2021; Ahlvist et al., 2012; Beckervordersandforth et al.,
76 2017; Homem et al., 2014; Khacho et al., 2016; Knobloch et al., 2013; Knobloch et al., 2017;
77 Namba et al., 2020; Prozorovski et al., 2008; Stoll et al., 2015; Xie et al., 2016), suggesting that a
78 rewiring of energy metabolism plays important roles over NSPC fate decisions as it has been
79 proposed for hematopoietic, immune and cancer cells (Mehta et al., 2017; Nakamura-Ishizu et al.,
80 2020; Puleston et al., 2017; Snaebjornsson et al., 2020). Yet, besides overall state-dependent
81 changes in nuclear gene transcription (Llorens-Bobadilla et al., 2015; Shin et al., 2015) it remains
82 unclear how the reversibility of these metabolic programs is coordinated at the level of single
83 organelles in adult NSPCs.

84 In this study, we simultaneously investigated the changes in energy metabolism and
85 mitochondrial protein network dynamics underlying the activity of adult NSPCs. By using a
86 combination of unbiased omics approaches and conditional mouse models, we identified the *i*-
87 AAA protease YME1L for being central in acutely shaping the mitochondrial proteome of NSPCs
88 between active and quiescent states. Specifically, we demonstrated that YME1L contributes to
89 rewire mitochondrial metabolism to sustain NSPC proliferation. By genetically manipulating
90 YME1L activity *in vitro* and *in vivo*, we showed that this effect is independent from mitochondrial
91 dynamics. Rather, this rewiring process impacts the rate of mitochondrial fatty acid catabolism

92 (FAO) to sustain the production of tricarboxylic acid (TCA) cycle intermediates and nucleotide
93 biosynthesis, which we showed to be necessary for NSPC proliferation. By lineage analysis of
94 NSPC at the single clone level *in vivo*, we demonstrated that lack of YME1L affects stem cell fate
95 by limiting self-renewal and promoting premature differentiation, ultimately causing NSPC pool
96 depletion.

97

98 **Results**

99 **YME1L proteolytic activity mirrors opposed metabolic states in adult NSPCs**

100 To reveal dynamics of protein networks underlying reversible, state-dependent changes in fuel
101 utilization of adult NSPCs, we combined an unbiased proteomic approach with metabolomics
102 (Figure 1A). NSPCs were isolated from the adult hippocampal sub-granular zone (SGZ) and
103 maintained *in vitro* in either active proliferation (aNSPC) or quiescence (qNSPC), the latter state
104 induced via addition of bone morphogenetic protein 4 (BMP4) (Mira et al., 2010) (Figure 1A and
105 1B). By principal component (PCA) and protein distribution analyses, the proteome of qNSPCs
106 could be easily separated from that of aNSPCs and ex-qNSPCs (i.e., qNSPCs in which BMP4 had
107 been withdrawn to disclose reversible changes in the proteome) (Figures S1A and S1B).
108 Furthermore, we validated the expression of well-established markers matching with quiescent and
109 active NSPC states (Figure S1C), as well as the ability of aNSPCs to differentiate into beta-3
110 tubulin+ neurons following growth factors withdrawal from the proliferation media (Figure S1D).
111 Ingenuity Pathway Analysis (IPA) of this proteomic dataset revealed a number of differentially
112 regulated proteins with pathways associated to cell cycle control, nucleotide excision repair, gene
113 transcription and purine biosynthesis that were preferentially enriched in aNSPCs (Figure 1C). In
114 contrast, besides expected categories linked to phagosome/lysosome and autophagy (Leeman et
115 al., 2018), qNSPCs appeared particularly enriched in metabolic pathways, specifically
116 mitochondrial OXPHOS as well as fatty acid beta-oxidation (FAO) (Figure 1C), a catabolic
117 pathway which has been recently implicated in regulating adult NSPC behaviour (Knobloch et al.,
118 2017; Stoll et al., 2015). Hierarchical clustering of our dataset revealed conspicuous yet largely
119 reversible changes in the mitochondrial proteome (i.e., proteins annotated according to MitoCarta
120 3.0) (Rath et al., 2021) of NSPCs shifting from proliferation to quiescence within virtually each
121 mitochondrial compartment (Figure 1D). We identified 307 mitochondrial proteins for being
122 significantly changed (adjusted p-value < 0.05) between aNSPCs and qNSPCs, of which 64.2%

123 were up-regulated and 35.8% down-regulated. In particular, the steady-state levels of most FAO
124 enzymes, several OXPHOS proteins as well as TCA cycle enzymes appeared differentially
125 regulated between aNSPCs and qNSPCs (Figure 1D). While assessment of mitochondrial
126 membrane potential between qNSPCs and aNSPCs disclosed overall unchanged levels (Figure
127 S1E), single protein analysis confirmed that the relative abundance of many OXPHOS subunits,
128 particularly of complexes I, IV and V as well as that of enzymes regulating mitochondrial FAO
129 and TCA cycle metabolism was significantly higher in qNSPCs (Figures S1F-S1H), while their
130 expression to large degree reversed following BMP4 withdrawal. Consistent with these data,
131 metabolomics tracing analysis following feeding of qNSPCs with either $^{13}\text{C}_6$ -Glucose or $^{13}\text{C}_{16}$ -
132 Palmitate confirmed a higher flux for fatty acids as a carbon source to fuel TCA cycle metabolism
133 in comparison to glucose (Figure S1I).

134 To understand whether these proteome dynamics may mirror corresponding changes in
135 gene expression, we performed a comparative transcriptomic analysis of active versus quiescent
136 NSPCs (Figures 1E and S1J). Analysis of genes encoding for mitochondrial proteins revealed that
137 a total of 241 genes underwent significant changes (i.e., with a p-value < 0.05 and a \log_2
138 (fold change) > 0.5), with 39.4% being up-regulated and 60.6% down-regulated. Interestingly, the
139 observed proteomic changes of several TCA cycle enzymes and OXPHOS subunits, and in
140 particular of most FAO proteins, were poorly mirrored at the transcript level (Figure S1F-S1H and
141 S1K). In contrast, analysis of glycolytic enzymes - which reside in the cytosol - disclosed a much
142 higher correlation between protein and corresponding mRNA levels (Figure S1K). This suggests
143 that acute switches in NSPC metabolic states may be regulated by compartmentalized changes in
144 mitochondrial protein networks independent from gene transcription.

145 The turn-over of several classes of proteins in mitochondria is regulated by the proteolytic
146 activity of proteases distributed across sub-mitochondrial compartments (Quiros et al., 2015).
147 While mitochondria utilize these proteases to broadly preserve mitochondrial proteostasis and
148 function, accruing evidence supports additional roles in acutely shaping the mitochondrial
149 proteome to match specific metabolic needs (Deshwal et al., 2020). Among all detected
150 mitochondrial proteases in our proteomic dataset, only five of them (i.e., PITRM1, YME1L,
151 METAP1D, LACTB and HTRA2) disclosed significant changes between the examined NSPC
152 activity states (Figures 1F and S2A). Of these, a striking state-dependent and fully reversible
153 switch in the levels of the *i*-AAA peptidase YME1L caught our attention, with qNSPCs displaying

154 a significant reduction of this protein as compared to both aNSPCs and ex-qNSPCs (Figure 1F).
155 We independently validated YME1L protein to accumulate at decreased levels in qNSPCs (Figure
156 S2B), however this change was not mirrored by a transcriptional down-regulation, as *Yme1l*
157 mRNA appeared mildly yet significantly increased during quiescence (Figure 1G). YME1L is an
158 inner mitochondrial membrane peptidase whose mutation in humans causes brain disorders,
159 intellectual disability and optic nerve atrophy (Hartmann et al., 2016). YME1L has been implicated
160 in the proteolytic control of numerous mitochondrial substrates (MacVicar et al., 2019) including
161 the GTPase OPA1, whose regulated processing by both YME1L and OMA1 controls inner
162 mitochondrial fusion dynamics (Anand et al., 2014; Griparic et al., 2007; Song et al., 2007).
163 Because of its proteolytic activity, YME1L has been proposed to link mitochondrial dynamics to
164 proteostasis regulation in somatic tissues (Mishra et al., 2014; Sprenger et al., 2019; Wai et al.,
165 2015) and recently to metabolic reprogramming of mitochondria during hypoxia and starvation in
166 cell lines (MacVicar et al., 2019). YME1L mode-of-action involves its own autocatalytic
167 processing when highly active, which leads to a conspicuous reduction of both, YME1L direct
168 substrates and YME1L protein itself (Hartmann et al., 2016; MacVicar et al., 2019). Intriguingly,
169 previously validated mitochondrial targets of YME1L (e.g., PRELID1 and TIMM17a)
170 accumulated at strongly reduced levels in qNSPCs (Figure S2B), thus suggesting increased
171 YME1L-mediated proteolytic degradation of substrate proteins in qNSPCs alongside increased
172 YME1L autocatalytic turnover. To validate this possibility, we took advantage of *Yme1l*^{lox/lox} mice
173 (Anand et al., 2014) to isolate and grow *in vitro* NSPCs followed by treatment with an AAV
174 expressing Cre-GFP to induce *Yme1l* gene deletion (hereafter referred to as *Yme1l*^{CKO} NSPCs)
175 (Figure S2C). As expected, Cre expression resulted in the virtual disappearance of the endogenous
176 YME1L protein alongside an increase in the steady-state levels of its substrates PRELID1 and
177 TIMM17a, regardless of NSPC growing conditions (i.e., cells maintained in either proliferating or
178 quiescent media) (Figure 1H). Importantly, while AAV-mediated over-expression of wild-type
179 YME1L (*Yme1l*^{WT}) in *Yme1l*^{CKO} NSPCs restored PRELID1 and TIMM17a proteolytic processing
180 in a state-dependent manner (that is, higher processing in qNSPCs), expression of a mutated,
181 proteolytically-inactive YME1L variant (*Yme1l*^{E543Q}) (MacVicar et al., 2019), proved ineffective
182 (Figure 1H). Thus, we conclude that a differential YME1L proteolytic activity in adult NSPCs
183 reflects the acquisition of distinct metabolic states.

184

185 **YME1L is required for mitochondrial proteome rewiring between NSPC states**

186 We next examined in our proteomic dataset the levels of additional mitochondrial proteins which
187 have been recently proposed as likely substrates of YME1L in mouse embryonic fibroblasts
188 (MEFs) (MacVicar et al., 2019). Of these, we identified 22 recently annotated class I targets
189 (namely, putative substrates fulfilling stringent criteria) and 24 additional putative substrates
190 previously designated as class II (MacVicar et al., 2019). These include enzymes regulating
191 mitochondrial protein import, lipid transport, dynamics (i.e., the GTPase OPA1), solute carriers,
192 respiration and other metabolic functions (Figures 1I and S2D). Several of these proteins,
193 particularly those designated as class I, accumulated at visibly reduced levels specifically in
194 qNSPCs (Figure 1I). However, transcriptomic analysis revealed that collectively there were minor
195 or no changes in the corresponding mRNA levels of these genes between qNSPCs and aNSPCs
196 (Figure 1J). In contrast, non-mitochondrial markers known to be preferentially expressed in either
197 active or quiescent states displayed matched changes at both mRNA and protein levels (Figure 1J
198 and S1C). Interestingly, some of the putative YME1L substrates appeared to be only moderately
199 reduced or in certain cases (particularly in class II) even upregulated (Figures 1I and S2D). This
200 may reflect a certain cell type-specificity of the proteolytic activity of YME1L in adult NSPCs as
201 compared to MEFs (MacVicar et al., 2019), or further layers of regulation beyond protein turnover
202 as exemplified by several of class II putative substrates, whose expression in NSPCs consistently
203 differed at both the mRNA and protein levels (Figures S2D and S2E).

204 To gain further insights into the potential cell-type specificity of identified class I YME1L
205 substrates in NSPCs, we took advantage of *Yme1l*^{cKO} NSPCs and performed a proteomic analysis
206 utilizing as controls *Yme1l*^{lox/lox} NSPCs treated with an AAV expressing only GFP (Figure S2C).
207 At the mitochondrial level, *Yme1l* deletion caused the significant accumulation of most previously
208 annotated class I substrates which we identified for being specifically downregulated in wild-type
209 qNSPCs (Figure 2A), consistent with their turn-over being under the proteolytic control of
210 YME1L. We defined this subset as NSPC-specific, putative YME1L substrates (Figure S2F).
211 Accordingly, transcriptomic analysis of *Yme1l*^{cKO} NSPCs revealed that the mRNA levels of these
212 substrates remained virtually unchanged (Figure 2B). By contrast, very few of the previously
213 annotated class II substrates underwent any visible accumulation at the protein level following
214 *Yme1l* deletion (Figure S2G), confirming that YME1L substrate specificity may indeed be
215 regulated in a cell type-specific manner.

216 Next, we investigated the significance of the NSPC state-dependent asymmetry in YME1L
217 activity. We reasoned that *Yme1l* conditional deletion would provide a valid approach to
218 irreversibly interfere with the pronounced YME1L proteolytic activity that specifically identifies
219 the quiescent state in NSPCs (Figure 1H). *Yme1l* deletion was validated at the protein level and by
220 the marked accumulation of one of its direct targets (PRELID1) (Figures S2H and S2I). As
221 expected, we also observed stress-induced OPA1 processing by the peptidase OMA1 as indicated
222 by the accumulation of S-OPA1 forms c and e and the virtual lack of S-OPA1 form d, which results
223 from specific YME1L cleavage (Figure S2H) (Anand et al., 2014). In line with an increased OPA1
224 processing, morphological analysis of *Yme1l*^{cKO} NSPCs *in vitro* revealed a fragmented and
225 condensed mitochondrial network in comparison to control NSPCs (Figure S2J), which was also
226 mirrored by a visibly reduced proliferative capacity in *Yme1l*^{cKO} NSPCs (Figures S2K and S2L).
227 Conspicuously, NSPC proliferation was not restored in double-knockout *Yme1l/Oma1*^{cKO} NSPCs
228 (Figures S2K and S2L), in which OPA1 cleavage (by both YME1L and OMA1) is virtually
229 abolished and thus mitochondrial fusion as well as network tubulation restored (Figure S2J)
230 (Anand et al., 2014; Wai et al., 2015). Thus, YME1L appears to be required for sustaining adult
231 NSPC proliferation *in vitro* via mechanisms seemingly independent of its role in OPA1 processing
232 and the regulation of mitochondrial morphology (Iwata et al., 2020; Khacho et al., 2016).

233 Analysis of the proteomic landscape in *Yme1l*^{cKO} NSPCs revealed the unexpected lack of
234 any significant shift in the mitochondrial proteome between active (proliferating) and quiescent
235 conditions, as otherwise observed in wild-type NSPCs (Figure 2C). Intriguingly, hierarchical
236 cluster analysis and PCA showed that, regardless of culture media conditions, *Yme1l* deletion led
237 to a broad rewiring of the mitochondrial proteome beyond class I substrates, which was consistent
238 with the acquisition of a mitochondrial “state” more similar to control NSPCs shortly exposed (2
239 days) to pro-differentiating conditions (dNSPCs) (Figure 2D and 2E). In marked contrast to
240 *Yme1l*^{cKO} NSPCs, deletion of the protease *Oma1* only led to negligible changes in the
241 mitochondrial proteome of NSPCs (Figure S2M), indicating that the observed proteomic rewiring
242 was specific to *Yme1l* deletion. This apparent shift towards a differentiated-like state of *Yme1l*^{cKO}
243 NSPCs (Figure 2E) was reflected by the up-regulation of some neuron- (TUBB3, CAMK2B and
244 RAB3B) as well as astrocyte-specific (CX43, MLC1, ALDH1L1) markers even when *Yme1l*^{cKO}
245 NSPCs were specifically maintained in proliferating or quiescent media, contrary to control
246 NSPCs in which this pattern was exclusively induced after beginning of the differentiation protocol

247 (Figure 2F). Although *Yme1l*^{cKO} NSPCs did not spontaneously differentiate into neurons (as
248 assessed by morphology and marker expression), analysis of TUBB3 (i.e., β -3 tubulin)
249 immunoreactivity in cells maintained under proliferative media revealed a consistent up-regulation
250 in comparison to control NSPCs (Figure 2G and 2H), suggesting that *Yme1l* deletion may facilitate
251 neuronal differentiation under proper media conditions. Supporting this prediction, *Yme1l*^{cKO}
252 NSPCs exposed shortly (2 days) to differentiation media (Figure 2I) underwent an accelerated
253 differentiation into β -3 tubulin⁺ neurons at the expenses of residual proliferation (Figures 2J and
254 2K). Together, these data indicate that *Yme1l* deletion is sufficient to elicit broad changes in
255 mitochondrial proteome dynamics consistent with the reduction in NSPC proliferation and a shift
256 towards a differentiated-like state.

257

258 **Loss of YME1L in NSPCs impairs fatty acid-dependent metabolic flux into the TCA cycle 259 and leads to dNTP pool depletion**

260 Direct comparison of the mitochondrial proteome between *Yme1l*^{cKO} and control NSPCs
261 (maintained under either quiescent or active conditions) disclosed a down-regulation of proteins
262 falling into the FAO category (Figure 3A). In contrast, deletion of *Oma1* did not visibly affect the
263 expression levels of FAO enzymes (Figure S3A). Likewise, analysis of the mitochondrial
264 proteome in NSPCs lacking *Mitofusin1* (*Mfn1*) or *Mfn2* revealed that a collective down-regulation
265 of FAO proteins alongside defects in NSPC proliferation did not necessarily reflect a cellular state
266 characterized by mitochondrial fragmentation (Figures S3B-3D). Specifically, *Yme1l*^{cKO} NSPCs
267 failed in up-regulating FAO proteins when exposed to quiescent conditions (Figure 3B), despite
268 unchanged or even slightly up-regulated mRNA levels of the corresponding FAO genes (Figure
269 3C). Thus, while FAO enzymes do not appear to be under the direct control of YME1L proteolytic
270 activity, these data suggest that *Yme1l* deletion prevents the proteomic rewiring underlying key
271 switches in mitochondrial fuel utilization between NSPC activity states. To validate this
272 hypothesis, we first utilized SeaHorse analysis to examine oxygen consumption rates in *Yme1l*^{cKO}
273 NSPCs. While basal respiration was not affected as compared to control NSPCs, we found a
274 selective impairment in maximal and spared respiratory capacities when cells were fed with
275 palmitate, but not glucose (Figures 3D and 3E). Interestingly, glucose feeding experiments showed
276 that *Yme1l*^{cKO} NSPCs could achieve even higher peaks of respiration rates than control NSPCs
277 (Figures 3E) and that there were no deficits in the NAD/NADH ratio (Figure S3E), indicating that

278 OXPHOS capacity in these cells was likely not primarily impaired. Supporting this notion,
279 mitochondrial membrane potential assessed by Tetramethylrhodamine methyl ester (TMRM)
280 revealed no major changes in the average signal intensity between *Yme1l*^{cKO} and control NSPCs,
281 despite obvious alterations in mitochondrial morphology (Figures 3F and 3G). Likewise,
282 ultrastructural analysis of *Yme1l*^{cKO} NSPCs disclosed that fragmented mitochondria retained
283 cristae (Figure 3H) indicating that, similar to other cellular systems (Sprenger et al., 2019; Wai et
284 al., 2015), *Yme1l* deletion is not associated to mitochondrial dysfunction and aberrant ultrastructure
285 in adult NSPCs.

286 To further dissect the consequences of *Yme1l* deletion for NSPC mitochondrial
287 metabolism, we analysed isotope labelling of TCA cycle intermediates and associated newly-
288 synthetized amino acids by metabolomics following feeding with either ¹³C₁₆-Palmitate or ¹³C₆-
289 Glucose. We found that labelling of most TCA cycle metabolites was consistently and specifically
290 reduced in *Yme1l*^{cKO} NSPCs fed with ¹³C₁₆-Palmitate (Figure 4A), while of the quantified amino
291 acids only aspartate and glutamate appeared to be significantly affected (Figure 4B). In contrast,
292 the ¹³C₆-Glucose flux into the TCA cycle of *Yme1l*^{cKO} NSPCs appeared to remain stable or even
293 somewhat enhanced (Figures 4A and 4B). Importantly, quantification of total TCA cycle
294 metabolites revealed no collective changes besides a reduction in the content of citrate and
295 isocitrate (Figure S3I), arguing against a general dysfunction of the TCA cycle and confirming an
296 overall lower flux of specifically ¹³C₁₆-Palmitate into TCA cycle metabolites (Figures 4A). Also,
297 besides mild changes in total glycolytic metabolites (Figure S3H) *Yme1l*^{cKO} NSPCs fed with
298 glucose displayed a higher labelling of alanine, pyruvate and lactate (Figure S3F), which was
299 reflected by a higher extracellular acidification rate (ECAR) when cells were examined by
300 Seahorse (Figures S3G). Together, these data point to a general metabolic rewiring taking place in
301 *Yme1l*^{cKO} NSPCs, and support a defective feeding into the TCA cycle of specifically fatty acid
302 carbon units.

303 The selective reduction in aspartate and glutamate in NSPCs that were fed with palmitate
304 (Figure 4B) raised the possibility that the proliferation defects observed in *Yme1l*^{cKO} NSPCs may,
305 at least in part, result from reduced levels of nucleotides, which are required for cell proliferation
306 and specifically rely on the precursors aspartate and glutamate for their biosynthesis (Schoors et
307 al., 2015). Indeed, the steady-state levels of purine and pyrimidine deoxyribonucleotides (dNTPs)
308 were markedly reduced in absence of YME1L (Figure 4C). Consistent with a defective FAO-

309 dependent supply of carbon units for dNTPs biosynthesis, supplementation of exogenous dNTPs,
310 acetate or even aspartate to *Yme1l*^{cKO} NSPCs mostly restored dNTP levels, albeit at different
311 degrees (Figure 4C). To assess whether manipulation of dNTP content would be sufficient to
312 reactivate NSPC proliferation following *Yme1l* deletion, we then examined EdU incorporation
313 while maintaining NSPCs in proliferating media. Intriguingly, the tested compounds significantly
314 improved *Yme1l*^{cKO} NSPC proliferative capacity (Figures 4D and 4E) indicating that, *in vitro*,
315 manipulation of the dNTP pool can effectively compensate for the metabolic alterations of
316 *Yme1l*^{cKO} NSPC. Thus, *Yme1l* deletion drives NSPCs away from FAO-dependent metabolic
317 states, causing the subsequent depletion of dNTP precursors required to sustain NSPC
318 proliferation.

319

320 **YME1L is required for adult NSPC proliferation *in vivo***

321 To circumvent the limitations imposed by an *in vitro* system and defined media conditions,
322 we next addressed the role of YME1L in adult NSPCs *in vivo* by crossing *Yme1l*^{lox/lox} mice with a
323 line harbouring an hGFAP-driven, tamoxifen-inducible Cre^{ER} recombinase (Chow et al., 2008).
324 To reveal putative changes in NSPC mitochondrial morphology induced by Cre recombination,
325 which would be indicative of *Yme1l* deletion, we bred the resulting line with a mitochondrial-
326 targeted yellow fluorescent protein (mtYFP) reporter mouse (Sterky et al., 2011) (Figures 5A and
327 S4A). Analysis of NSPCs in the SGZ of the resulting *Yme1l*^{cKO} mice at 1 month following
328 tamoxifen administration disclosed a striking fragmentation of their mitochondrial network, in
329 contrast to control NSPCs, which retained a heterogeneous yet overall tubular network (Figure
330 5B). Intriguingly, simultaneous deletion of both *Yme1l* and *Oma1* in double-floxed animals mostly
331 restored a tubular mitochondrial morphology (Figure 5B), validating our results *in vitro* (Figure
332 S2J) that the fragmentation phenotype observed in *Yme1l*^{cKO} NSPCs is to large degree mediated
333 by stress-induced activation of OMA1 followed by excessive OPA1 processing (Anand et al.,
334 2014; Sprenger et al., 2019; Wai et al., 2015). Next, we examined the proliferative capacity of
335 adult *Yme1l*^{cKO} NSPCs. By 4 weeks after Cre-mediated recombination, EdU incorporation
336 experiments (Figure 5A) revealed a significant reduction in the number of proliferating NSPCs of
337 *Yme1l*^{cKO} mice both within the SGZ (Figures 5C and 5D) and sub-ventricular zone (SVZ) lining
338 the lateral ventricles (Figures S4E and S4F), the second major neurogenic niche in the adult murine
339 brain. This finding was corroborated by expression analysis of the endogenous proliferative marker

340 Ki67 in SOX2+ NSPCs within the SGZ of the dentate gyrus (Figures S4G-S4I). Interestingly,
341 while no proliferation changes were observed in *Oma1*^{cKO} mice (Figures S4B-S4D), simultaneous
342 deletion of both *Yme1l* and *Oma1* produced the same defect observed in *Yme1l*^{cKO} mice (Figures
343 5C, 5D and S4E-S4I), confirming this phenotype to be mediated by an YME1L-specific metabolic
344 function and ruling out possible primary effects caused solely by alterations in mitochondrial
345 fusion dynamics (Iwata et al., 2020; Khacho et al., 2016). Supporting these findings, AAV-
346 mediated re-expression of wild-type YME1L (*Yme1l*^{WT}) in *Yme1l*^{cKO} NSPCs *in vitro* (Figures
347 S5A) or *in vivo* via intracranial delivery into the DG (Figures 5E and S5B-S5D) significantly
348 restored NSPC proliferation and mitochondrial morphology, in contrast to expression of a mutated,
349 proteolytically-inactive YME1L variant (*Yme1l*^{E543Q}), which proved ineffective. Interestingly,
350 forced expression of *Yme1l*^{E543Q} alone was sufficient to reduce NSPC proliferation in control mice
351 (Figure 5E), suggestive of a dominant negative effect. Subsequent analysis of Ki67⁺ cells in
352 *Yme1l*^{cKO} animals treated with EdU 4 days earlier (Figure S5E) revealed a marked reduction in
353 the percentage of EdU-retaining NSPCs that were still proliferating at the time of sacrifice
354 compared to control mice (12.6% in *Yme1l*^{cKO} mice vs. 42.9% in controls) (Figures S5F-S5H),
355 demonstrating that lack of YME1L severely affected NSPC pool amplification. To understand
356 whether NSPC proliferation dynamics were already altered at times earlier than 4 weeks following
357 Cre-mediated *Yme1l* deletion, mice were treated with EdU at 5-6 days after tamoxifen
358 administration and examined 4 days later (Figure 5F). Analysis revealed unchanged numbers of
359 Nestin⁺ cells and a trend towards a reduced total density of EdU⁺ cells, which manifested as a
360 significant drop of EdU incorporation into Nestin⁺ cells (Figure 5G and 5H). Thus, these data are
361 consistent with an early proliferative defect in Nestin⁺ NSPC that persisted later on.

362

363 ***Yme1l* conditional deletion impairs adult NSPC self-renewal and promotes pool depletion**

364 To gain further insights into the consequences of *Yme1l* deletion for NSPC fate, we
365 generated inducible *Yme1l*^{cKO} mice in which Cre recombination is conditionally controlled by the
366 Nestin promoter (Nestin::Cre^{ERT2}) (Lagace et al., 2007) and utilized a cytosolic tdTomato reporter
367 line (Madisen et al., 2010) to fate map any resulting progeny from recombined radial glia-like
368 (RGL) NSPCs. Mice were treated with tamoxifen for 5 consecutive days, in order to label the
369 majority of NSPCs and their immediate neuronal progeny during their first month of maturation
370 (Figure 6A). In line with our EdU experiments (Figure 5D), analysis revealed a drastic reduction

371 in the total density of tdTomato^+ cells in $\text{Yme1l}^{\text{cKO}}$ mice as compared to control littermates (Figure
372 6B). Specifically, the density of Sox2^+ RGL NSPCs (namely, type I cells) as well as that of Tbr2^+
373 (type II) cells and newly-generated Dcx^+ immature neurons was significantly reduced (Figure 6C,
374 S6A and S6B), confirming that neurogenesis was impaired. In contrast, the density of new neurons
375 transiting from immature to mature stages ($\text{Dcx}^+/\text{NeuN}^+$) as well as that of NeuN^+ neurons that
376 had just matured appeared similar between the two groups at this relatively early time of 1 month
377 post-recombination (Figure 6C). Also, the relative proportion of NeuN^+ neurons among all
378 neuronal maturational stages was not visibly different compared to that of control mice (Figure
379 6D), suggesting that neuronal maturation was not primarily affected in absence of Yme1l and
380 consistent with a putative progressive depletion of NSPCs in favour of premature differentiation.
381 Supporting this notion, cell density analysis performed at 3 months after tamoxifen administration
382 disclosed a marked impairment in the generation and subsequent network addition of further
383 NeuN^+ new neurons (Figure 6C), indicating cumulative defects in neurogenesis driven by
384 exhaustion of the NSPC pool.

385 To ascertain the specific consequences caused by Yme1l deletion for NSPC behaviour, we
386 performed a clonal analysis *in vivo* by targeting few individual RGL NSPCs within each
387 hippocampi (Bonaguidi et al., 2011). Low titre tamoxifen treatment in $\text{Yme1l}^{\text{cKO}}$ mice resulted in
388 sparse labelling of isolated RGL NSPCs (Figures S6C and S6D), which allowed us to monitor their
389 activity and progression along the lineage at the level of individual clones (Figure 6E).
390 Specifically, cell composition within isolated clones revealed whether recombined RGL NSPCs
391 had remained quiescent, underwent division (symmetrically or asymmetrically) and if they became
392 eventually depleted from the clone over the course 1 month (Figure 6D). Detailed analysis of clone
393 composition showed that while control and Oma1^{cKO} tdTomato^+ clones were in average larger in
394 size (Figure S6E) and possessed a mixed combination of neurons, astrocytes and RGL NSPCs
395 (referred to as R), which is indicative of NSPC being able to self-renew (Figures 6F and 6H), the
396 majority (over 50%) of $\text{Yme1l}^{\text{cKO}}$ clones were entirely devoid of any R (indicative of NSPC pool
397 depletion) (Figures 6F and 6G). By further examining the remaining fraction of clones still
398 containing Rs, we found that in average $\text{Yme1l}^{\text{cKO}}$ clones contained 1.15 ± 0.06 Rs per clone (109
399 Rs in 99 clones in total from 8 animals), in contrast to control (71 Rs in 47 clones in total from 7
400 animals) and Oma1^{cKO} (117 Rs in 80 clones in total from 8 animals) clones, which contained in
401 average 1.5 ± 0.03 and 1.35 ± 0.07 Rs per clone, respectively (Figure 6H, inset). In particular, the

402 relative proportion of R doublets (i.e., purely amplifying clones) as well as neurogenic clones (i.e.,
403 containing R and neurons) were significantly reduced in *Yme1l*^{cKO} animals (11% amplifying
404 clones in *Yme1l*^{cKO} versus 30% in control mice; and 22% neurogenic clones in *Yme1l*^{cKO} versus
405 ~41% in control mice) (Figure 6H). Thus, *Yme1l* deletion compromises adult NSPC self-renewal
406 capacity and pool maintenance, ultimately impacting neurogenesis.

407

408 **Discussion**

409 Owing to their functional heterogeneity, the fate of NSPCs in the mouse DG can have different
410 outcomes. In young adult mice, a significant fraction of NSPCs undergoes a limited number of
411 self-renewing divisions interspersed by temporary quiescent states, before being eventually
412 depleted (Bonaguidi et al., 2011; Encinas et al., 2011; Pilz et al., 2018). However, populations of
413 NSPCs with extended periods of quiescence favouring long-term self-renewing capacity exist, and
414 likely critically contribute to continuous neurogenesis during adulthood (Bottes et al., 2021; Harris
415 et al., 2021; Ibrayeva et al., 2021). By examining changes in the mitochondrial proteome mirroring
416 the acquisition of active and quiescent states, we have identified an unexpected role for the protease
417 YME1L in maintaining the self-renewing potential of adult NSPCs seemingly independent from
418 its role in balancing mitochondrial dynamics via OPA1 processing (Anand et al., 2014; Wai et al.,
419 2015). Mitochondrial fission/fusion dynamics have an instructing role in regulating the fate of
420 NSPCs and early post-mitotic cells during embryonic cortical development, with fusion promoting
421 self-renewal and mitochondrial network fragmentation favouring differentiation (Iwata et al.,
422 2020; Khacho et al., 2016). Intriguingly, by simultaneously manipulating *Yme1l* and *Oma1* in adult
423 NSPCs we restored a tubular mitochondrial network in absence of YME1L and revealed YME1L-
424 specific effects beyond changes in mitochondrial morphology. These are consistent with a broader
425 proteolytic function of YME1L in shaping the mitochondrial proteome to instruct and
426 accommodate specific metabolic adaptations of NSPCs, as recently observed in cell lines exposed
427 to hypoxia or starvation, conditions that promote a metabolic shift towards OXPHOS-independent,
428 glycolytic growth and are of relevance for certain types of cancer (MacVicar et al., 2019). Different
429 from immortalized embryonic fibroblasts and cancer cell lines, however, we found a significant
430 degree of NSPC specificity in the proteolytic activity of YME1L, as revealed by the assessment
431 of putative direct substrates accumulating following *Yme1l* deletion. For instance, most previously
432 annotated class II substrates (MacVicar et al., 2019) did not appear to be under the direct (or

433 unique) control of YME1L processing in adult NSPCs. These include the mitochondrial membrane
434 transporter SLC25A33, whose up-regulation in *Yme1l*-deficient cell lines was recently linked to
435 mitochondrial DNA release into the cytosol with ensuing inflammatory response and marked
436 activation of interferon-stimulated genes (Sprenger et al., 2021), of which we found no evidence
437 in adult *Yme1l*^{cKO} NSPCs (Figure S3J). Thus, although it remains conceivable that additional
438 NSPC-specific substrates may exist beyond those initially proposed by MacVicar et al., it appears
439 that YME1L activity is differentially regulated in a cell type- and, possibly, stimulus-specific
440 manner.

441 In our system, proteomics and metabolomics showed that YME1L is required to preserve
442 NSPC activity states, as lack of YME1L caused the irreversible shift of the mitochondrial proteome
443 towards a FAO-independent, differentiated-like state. Accordingly, *Yme1l*^{cKO} NSPCs displayed a
444 drop in proliferation *in vitro* and *in vivo*. *In vitro*, the resulting reduction in FAO rates observed in
445 absence of YME1L was found to be responsible for the overall drop in proliferation, even when
446 NSPCs were exposed to growth factors, indicating that *Yme1l*^{cKO} NSPCs attained an altered
447 metabolic state unable to respond to proliferative stimuli. Mechanistically, we identified the
448 feeding of fatty acid carbon units into TCA cycle-derived intermediates that were required to
449 sustain the dNTP pool as the bottleneck causing this proliferative phenotype, as exogenous
450 replenishment of either dNTPs or their precursors was sufficient to revert proliferation. Besides
451 impairing proliferation, *Yme1l* deletion in NSPCs resulted in an accelerated propensity to
452 differentiate into neurons when growth factors were withdrawn from the growing media *in vitro*
453 and once RGL NSPCs became activated *in vivo*. Strikingly, deletion of *Yme1l* at the single clone
454 level *in vivo* led to a phenotype reminiscent of the genetic ablation of FAO, which drives NSPC
455 exit from quiescence, potentiating terminal neurogenic symmetric divisions at the expenses of self-
456 renewal (Knobloch et al., 2017; Xie et al., 2016). Likewise, we found that over 50% of examined
457 *Yme1l*^{cKO} clones contained neurons (and astrocytes) but were devoid of any RGL NSPC, which is
458 consistent with NSPC pool depletion and in line with the metabolic alterations induced by
459 defective FAO.

460 Together, our results reveal YME1L for playing a critical role in acutely shaping the
461 mitochondrial proteome of NSPCs, adding an important layer of regulation in the mechanisms
462 governing NSPC metabolic state transitions beyond potential changes in gene expression
463 (Beckervordersandforth et al., 2017; Llorens-Bobadilla et al., 2015; Shin et al., 2015). Importantly,

464 our data indicate that switches in fuel utilization of adult NSPCs can be coordinated by
465 compartmentalized dynamics in protein networks, and suggest that the activity of mitochondrial
466 proteases critically contributes to regulate this form of metabolic plasticity.

467

468 **Limitations of study**

469 While our data emphasize the role of mitochondrial proteome rewiring in regulating NSPC
470 activity, an obvious limitation of our study is that the proteomics and metabolomics data presented
471 here were exclusively obtained from adult NSPCs isolated and maintained *in vitro*. Owing to
472 technological limitations that currently prevent to efficiently discriminate and sort distinct NSPC
473 activity states (e.g., active and quiescent) from brain tissue, it thus remains unclear to which extent
474 NSPCs adjust their mitochondrial proteome and metabolome in a state-dependent manner *in vivo*.
475 Assessing these changes *in vivo* may pose further challenges on account of distinct depths of
476 quiescence acquired by NSPCs during adulthood (Bottes et al., 2021; Harris et al., 2021; Ibrayeva
477 et al., 2021). Yet, with the advent of refined strategies suitable for single-cell mass spectrometry-
478 based proteomics (Brunner et al., 2021), further investigations should aim at reconstructing the
479 proteomic landscape heterogeneity of NSPC activity states *in vivo* as it has been shown at the
480 transcriptomic level utilizing single-cell RNA-seq approaches (Bottes et al., 2021; Harris et al.,
481 2021; Llorens-Bobadilla et al., 2015; Shin et al., 2015).

482

483 **Author contributions:** Conceptualization, G.A.W. and M.B.; Methodology, G.A.W., R.J.A.,
484 J.M.S., S.M., P.G., E.M. and M.B.; Investigation, G.A.W., H-G.S., K.N., S.C., D.S. and M.B.;
485 Formal analysis, G.A.W., H-G.S., K.N., R.J.A., S.M.V.K., D.S., S.M., P.G., E.M. and M.B.;
486 Writing - Original Draft, M.B.; Writing – Review and Editing, G.A.W., H-G.S., D.S., P.G., E.I.R.,
487 E.M., T.L. and M.B.; Resources, V.S., M.J., T.L. and M.B.; Funding Acquisition, E.I.R., E.M.,
488 T.L. and M.B.; Supervision, M.B.; Project Administration, M.B.

489

490 **Acknowledgments:** We thank N.G. Larsson for providing mitoYFP floxed-stop mice. B.
491 Fernando and T. Öztürk for excellent technical assistance. J. Matutat, G. Piper, D. Schneider and
492 the other members of the CECAD *in vivo* facility for excellent assistance. A. Schauss and all
493 members of the CECAD imaging facility for assistance with microscopes. C. Frese and the team

494 of the CECAD proteomics core facility for assistance. J. Altmüller and the team of the Cologne
495 Center for Genomics (CCG) for assistance with RNA-Seq procedures. This work was supported
496 by the Deutsche Forschungsgemeinschaft (SFB1218 - Grant No. 269925409, SFB1451 - Grant
497 No. 431549029 and CECAD EXC 2030 – Grant No. 390661388) and European Research Council
498 (ERC-StG-2015, grant number 67844) to M.B.; the Deutsche Forschungsgemeinschaft (SFB1218
499 - Grant No. 269925409) to T.L. and E.I.R.; and by the German-Israeli-Project (DIP, RA1028/10-
500 1) and the Max-Planck-Society to T.L. E.M. was supported by an Advanced Postdoc Grant
501 (Deutsche Forschungsgemeinschaft, SFB1218 - Grant No. 269925409).

502

503 **Author Information:** The authors declare no competing financial interests.

504

505

506

507

508

509

510

511

512

513

514

515

516

517

518

519

520

521

522

523

524

525

526 **STAR methods**

527 **Lead contact and materials availability**

528 Further information and requests for resources and reagents should be directed to and will be
529 fulfilled by the Lead Contact, Matteo Bergami (matteo.bergami@uk-koeln.de). All unique/stable
530 reagents generated in this study are available from the Lead Contact without restrictions. There are
531 restrictions to the availability of mice due to MTA.

532

533 **Experimental model and subject details**

534 Six to 8-week old C57BL/6 and transgenic mice of mixed genders were used in this study. Mice
535 were housed in groups of up to 5 animals per cage supplied with standard pellet food and water *ad*
536 *libitum* with a 12 h light/dark cycle, while temperature was controlled to 21-22°C. Mice carrying
537 the loxP-flanked genes *Yme1l*^{f1/f1}, *Omal*^{f1/f1} or both (Anand et al., 2014) were crossed with the
538 inducible hGFAP-Cre^{ERTM} (Chow et al., 2008) line and subsequently to the Cre-dependent
539 mitochondrial-targeted mtYFP reporter (Sterky et al., 2011). For clonal analysis experiments,
540 *Yme1l*^{f1/f1} or *Omal*^{f1/f1} mice were crossed with the Nestin-Cre^{ERT2} line (Lagace et al., 2007) in
541 combination with the inducible tdTomato reporter (Madisen et al., 2010). Mice carrying the loxP-
542 flanked genes *Mfn1*^{f1/f1} and *Mfn2*^{f1/f1} (Lee et al., 2012) were utilized exclusively for preparation of
543 NSPC cultures maintained *in vitro*. All experimental procedures were performed in agreement
544 with the European Union and German guidelines and were approved by the State Government of
545 North Rhine Westphalia.

546

547 **Method details**

548 Tamoxifen and EdU treatments. Mice were intraperitoneally injected with 4-hydroxytamoxifen
549 (40 mg/ml dissolved in 90% corn oil and 10% ethanol) once a day for a 5 consecutive days. For
550 clonal analysis, mice received a single injection of 0.4 mg. The exact time frames of individual
551 experiments are indicated in the text and figures. To examine NSPC proliferation, mice were given
552 5-ethynyl-2-deoxyuridine (EdU) via i.p. injections (25mg/ml, stock solution dissolved in 0.9%
553 saline) and sacrificed 2 hours or 4 days after the last injection.

554

555 Stereotactic procedures and viral injections. Mice were anesthetized by intraperitoneal injection
556 of a ketamine/xylazine mixture (100 mg/kg body weight ketamine, 10 mg/kg body weight

557 xylazine), treated subcutaneously with Carprofen (5 mg/kg) and fixed in a stereotactic frame
558 provided with a heating pad. A portion of the skull covering the somatosensory cortex (from
559 Bregma: caudal: -2.0; lateral: 1.5) was thinned with a dental drill avoiding to disturb the underlying
560 vasculature and small craniotomy sufficient to allow penetration of a glass capillary performed.
561 For virus injection a finely pulled glass capillary was then inserted through the dura (-1.9 to -1.8
562 from Bregma) and a total of about 500 nl of virus were slowly infused via a manual syringe
563 (Narishige) in multiple vertical steps spaced by 50 μ m each during a time window of 10-
564 20 minutes. After infusion, the capillary was left in place for few additional minutes to allow
565 complete diffusion of the virus. After capillary removal, the scalp was sutured and mice were
566 placed on a warm heating pad until full recovery. Physical conditions of the animals were
567 monitored daily to improve their welfare before euthanize them.

568

569 *Viral production.* Helper-free AAV vectors were either obtained from Addgene or produced
570 according to standard manufacturer's instructions (Cell Biolabs) as previously described (Göbel
571 et al., 2020). Briefly, 293AAV cells were transiently transfected with a transfer plasmid carrying
572 the desired transgenes along with a packing plasmid encoding the AAV1 capsid proteins and a
573 helper plasmid, using the calcium phosphate method. Crude viral supernatants were obtained via
574 lysing cells in PBS by freeze-thaw cycles in a dry ice/ethanol bath. The AAV1 vectors were
575 purified by discontinuous iodixanol gradient ultracentrifugation (24h at 32,000 rpm and 4°C) and
576 concentrated using Amicon ultra-15 centrifugal filter unites. Genomic titres were determined by
577 real-time qPCR. For generation of AAVs expressing Yme111^{WT} and Yme111^{E543Q}, the
578 corresponding previously described sequences (MacVicar et al., 2019) were subcloned into the
579 destination AAV plasmid and sequenced for validation before producing the final AAV.

580

581 *Immunohistochemistry.* Mice were anesthetized by intraperitoneal injection of a ketamine/xylazine
582 mixture (130 mg/kg body weight ketamine, 10 mg/kg body weight xylazine), transcardially
583 perfused with 4% PFA in PBS and the brain isolated. Following overnight post-fixation, coronal
584 brain sections (50 μ m thick) were prepared using a vibratome (Leica, VT1000 S) and
585 permeabilized in 1% Triton X-100 in PBS for 10 min at RT, followed by brief incubation in 5%
586 BSA and 0.3% Triton X-100 in PBS before overnight immunodetection with primary antibodies
587 diluted in blocking buffer at 4°C on an orbital shaker. The next day, sections were rinsed in PBS

588 3x 10 min and incubated for 2h at RT with the respective fluorophore-conjugated secondary
589 antibodies diluted in 3% BSA. After washing and nuclear counterstaining with 4',6-diamidino-2-
590 phenylindole (DAPI, ThermoFisher, 3 μ M), sections were mounted on microscopic slides using
591 Aqua Poly/Mount (Polysciences). The following primary antibodies were used: chicken anti-GFP
592 (1:500, Aves Labs, GFP-1020), rabbit anti-RFP (1:500, Rockland, 600401379), rabbit anti-GFAP
593 (1:500, Millipore, ab5804), mouse anti-GFAP (1:500, Millipore, MAB360), mouse anti-Tbr2
594 (1:300, Abcam, ab23345), guineapig anti-Dcx (1:1000, Millipore, AB2253), mouse anti-NeuN
595 (1:300, Millipore, MAB377) and mouse anti-Nestin (1:500, Millipore, MAB353). The following
596 secondary antibodies were used (raised in donkey): Alexa Fluor 488-, Alexa Fluor 546-, Alexa
597 Fluor 647- conjugated secondary antibodies to rabbit, mouse, chicken and rat (1:1000, Jackson
598 ImmunoResearch).

599

600 **Image analysis and quantification.** All images were acquired utilizing a SP8 Confocal microscope
601 (Leica Microsystems) equipped with 20x (NA 0.75), 40x (NA 1.3), 63x (NA 1.4) and 100x
602 (NA 1.3) immersion objectives, white light laser and multiple HyD detectors. For quantification
603 of cell proliferation and neurogenesis *in vivo*, six to eight coronal brain sections per brain
604 corresponding to similar anatomical locations across mice were used. All acquired z-stack images
605 (LAS software) were converted into TIFF files and analysis was performed off-line using the
606 ImageJ software (National Institute of Health, Bethesda, United States). Cells counting was
607 performed manually by using the Cell Counter plug in and by normalizing the number of marker+
608 cells over the volume of the DG or SVZ (measured area multiplied by the inter-stack interval). The
609 total number of RGL in the DG was obtained by examining their unique morphological features,
610 which makes them well distinguishable from other cell types (short radial process spanning the
611 granule cell layer, small body in the SGZ), and positivity for the marker GFAP. Likewise, the
612 number of neurons was assessed by unique morphological features (round cell body and a visible
613 dendritic arbor) as well as by the positivity for immature (Dcx) or more mature markers (NeuN).
614 For clonal analysis, the whole hippocampus was investigated through serial brain sections
615 (thickness 75 μ m), which were first screened for TdTomato+ cells with a 20x oil objective and then
616 z-stack acquisition of regions containing positive cells taken with a 20x and a 63x oil objectives.
617 For quantification, regions including the molecular layer (ML), granular cell layer (GCL), sub
618 granular zone (SGZ) and Hilus bordering the SGZ of the DG were considered. A radius of 150 μ m

619 from the RGL cell within the clone was used to determine the spatial limits of the clone itself
620 (Bonaguidi et al., 2011). Clones were categorized according to the presence or absence of RGL
621 and by the composition of other cell types (neurons and astrocytes). After initial validation by
622 marker expression of possible TdTomato+ cell types (see above), cell identity in individual clones
623 was determined based on morphology: RGL with a triangular-shaped soma located in the SGZ, a
624 short radial process branching in the inner molecular layer and absence of any axon; neurons for
625 having round cell body located in the GCL and clearly visible apical dendritic processes; and
626 protoplasmic astrocytes, for having a bushy morphology irrespective of their locations. For
627 imaging of mitochondria in RGL *in vivo*, mice bearing the mtYFP reporter were utilized, and z-
628 stack acquisitions of individual RGL in the upper blade of the DG (identified by location of their
629 soma in the SGZ and the presence of a distinct GFAP+ radial process) taken with a 63x oil
630 objective utilizing an inter-stack interval of 0.3 μ m. Following acquisition, images were processed
631 by deconvolution utilizing the Huygens Pro software (Scientific Volume Imaging) and rendered
632 in volumetric views to appreciate changes in mitochondrial morphology.

633

634 Mitochondrial membrane potential measurements. For membrane potential experiments *in vitro*,
635 seeded NSPCs were incubated with TMRM (25 nM) for 10 minutes in imaging media (124 mM
636 NaCl, 3 mM KCl, 2 mM CaCl₂, 1 mM MgCl₂, 10 mM HEPES, 10 mM D-glucose and pH 7.4),
637 followed by 1x washing and live imaging utilizing a confocal microscope (inverted Leica SP8,
638 40x oil objective) and a 560 nm excitation wavelength with a laser power inferior to 1%. Cells
639 were randomly selected for their positivity to the AAV-encoded GFP reporter (cytosolic GFP for
640 control cells, nuclear Cre-GFP for knock-out cells) as well as presence of TMRM staining and
641 acquired with identical parameters (laser power, zoom, resolution, scanning speed, pinhole, digital
642 gain and offset) for all conditions. Total TMRM signal was then quantified via ImageJ for
643 individual cells and normalized to the covered TMRM area to compensate for differences in
644 mitochondrial network morphology and size.

645

646 Electron microscopy. Cells were grown on aclar foil and fixed with a pre-warmed solution of 2%
647 glutaraldehyde, 2.5% sucrose, 3 mM CaCl₂, 100 Mm HEPES, pH 7.4 at RT for 30min and 4°C for
648 other 30 min. Cells were washed with 0.1 M sodium cacodylate buffer (Applichem), incubated
649 with 1%OsO₄ (Science Services), 1.25% sucrose and 10mg/ml potassium ferrocyanid in 0.1M

650 cacodylate buffer for 1 hour on ice, and washed three times with 0.1M cacodylate buffer.
651 Subsequently, cells were dehydrated using ascending ethanol series (50, 70, 90, 100%) for 7 min
652 each at 4°C. Afterwards, cells were incubated with ascending EPON series (Sigma-Aldrich) at
653 4°C, transferred to fresh EPON for 2h at RT and finally embedded for 72 hours at 62°C. Ultrathin
654 sections of 70 nm were cut using an ultramicrotome (Leica Microsystems, EM-UC7) and a
655 diamond knife (Diatome, Biel, Switzerland). Sections were put on copper grids (mesh 100, Science
656 Service) with formvar film and stained with uranyl acetate for 15 min at 37°C and lead nitrate
657 solution for 4 min. Electron micrographs were taken with a JEM-2100 Plus Transmission Electron
658 Microscope (JEOL), a OneView 4K 16 bit camera (Gatan) and the software DigitalMicrograph
659 (Gatan).

660

661 NSPCs isolation and cell culture experiments. Primary adult mouse NSPCs were isolated and
662 cultured as previously described (Walker and Kempermann, 2014). In brief, young adult mice (5-
6 week old) were quickly sacrificed by cervical dislocation and the brain isolated under sterile
663 conditions. The regions corresponding to the DG or SVZ of the lateral ventricles were
664 microdissected and collected in cold Neurobasal-A. The pooled tissue from 5-6 mice was chopped
665 with a scalpel into small fragments and incubated in pre-warmed Papain (2.5 U/ml), Dispase (1
666 U/ml) and DNase (250 U/ml) cocktail (PDD) enzyme mix for 20 min at 37°C. The cells were then
667 triturated 10-15 times with a fire-polished Pasteur pipette, collected by centrifugation for 5 min
668 (200g) at room temperature and enriched for the NSPC fraction using a 22% Percoll gradient. Cells
669 were washed twice in Neurobasal-A and plated in proliferation medium containing Neurobasal-A,
670 B27, Glutamax and FGF (1:2500) and EGF (1:2500) into Poly-D-lysine/Laminin coated single
671 wells in 24-well plate. NSPCs were passed when reaching about 80% confluence up to a maximum
672 of 17-18 passages. NSPCs were usually frozen between passages 5 to 6 and stored at -80°C for
673 further use. Experiments were performed with adult NSPCs grown as a monolayer and maintained
674 in proliferation medium. Quiescence was induced by replacing the proliferation medium with
675 medium containing Neurobasal-A supplemented with B27, Glutamax, human FGF-2 (20 ng/ml)
676 and BMP4 (50 ng/ml, 5020-BP-010, RnD System). Cells were maintained in quiescence medium
677 for 3 days before analysis. Quiescence was reversed by plating the quiescent NSPCs in normal
678 proliferating medium. For some experiments requiring substantial amounts of cells (metabolomics
679 and SeaHorse analyses) NSPCs were isolated from the SVZ of the corresponding floxed (or

681 double-floxed) mouse line, given the substantial higher amount of NSPCs that can be obtained
682 from this region as compared to the DG (Guo et al., 2012). NSPCs were seeded (2 X 10⁵ cells/well)
683 on 6 well plates in proliferating media pre-coated with Poly-D-lysine and experiments were
684 conducted by transducing cultures with AAVs expressing either Cre recombinase (AAV5-eGFP-
685 Cre, Addgene #105545) or GFP only (AAV5-eGFP, Addgene #105530). To compare proliferation
686 rates, cells were seeded (1 x10⁵ cells/well) on glass coverslips pre-coated with Poly-D-lysine and
687 Laminin in proliferation media supplemented with or without 5x dNTP mix, 20 mM sodium
688 acetate or 150 μ M L-Aspartic acid. After 48h, cells were treated with 20 μ M Edu and incubated 2h
689 followed by fixation with 4% PFA pre-warmed at room temperature for 5 mins. Cells were washed
690 3 times with 1X PBS followed by EdU staining using Click-iT EdU Imaging Kit (Invitrogen).

691

692 *Measurement of Oxygen consumption by XF96 SeaHorse microplate.* Oxygen consumption rate
693 (OCR) of intact NSPCs was determined using a Seahorse XF96 extracellular flux analyser. NSPCs
694 were seeded in coated XF96 cell culture microplate at 22,000 cells/well in 180 μ L of proliferation
695 media with 25mM Glucose. The following day, proliferation media was removed from each well
696 and cells were washed twice with assay medium consisting of (111mM NaCl, 4.7 mM KCl, 1.25
697 mM CaCl₂, 2mM MgSO₄, 1.2 mM NaH₂PO₄ 5mM HEPES) supplemented with 25 mM glucose.
698 Cells were incubated in 180 μ l medium at 37°C in a CO₂-free incubator for one hour prior to
699 measurements. OCR was monitored upon serial applications of oligomycin (2 μ M), FCCP (3 μ M)
700 and rotenone/antimycin A (0.5 μ M). The optimal FCCP concentration was determined by titration
701 (from 0.5 to 4 μ M) in separate experiments. To measure OCR under palmitate feeding, cells were
702 seeded as described above and 4 h after, the proliferation media was replaced with substrate-
703 limited proliferating medium (5mM glucose). 45 min prior the assay, cells were washed twice with
704 aCSF supplemented with 5mM glucose (FAO assay medium) and incubated in 150 μ L/well FAO
705 assay medium in a CO₂-free incubator for 30-45 min at 37°C. Just before the start of the assay the
706 media was replaced with 170 μ M XF Palmitate-BSA FAO substrate.

707

708 *Western blotting.* Cells were harvested in ice cold 1X PBS and homogenized in ice-cold RIPA
709 buffer (50 mM Tris-HCl, pH 7.4, 150 mM NaCl, 1% Triton X-100, 0.1% SDS, 0.05% sodium
710 deoxycholate, and 1 mM EDTA including protease inhibitor cocktail mix added freshly) by
711 triturating 20-25 times with 200 μ L pipette tip. The homogenized lysate was incubate at 4°C for 30

712 min followed by centrifugation at 10,000 rpm at 4°C for 10 min and supernatant was collected.
713 50µg of total protein was loaded in SDS-PAGE for separation, followed by transfer to
714 nitrocellulose membranes, and immunoblotting using the following primary antibodies (see Key
715 resource table for details): mouse anti-PRELID1, rabbit anti-YME1L, mouse anti-OPA1, rabbit
716 anti-TIMM17A, rabbit anti-TOMM20 and mouse anti-SDHA.

717

718 Proteomics sample preparation. Prior to protein extraction cells were washed using ice cold 1X
719 PBS. Cells were then lysed using 80 µL of 8 M Urea and stored at -80°C for further use. Protein
720 samples were sonicated to degrade the chromatin followed by centrifugation at 20,000 g for 15
721 min at 4°C and the supernatant was collected. Protein concentration was measured using the Direct
722 Detect spectrometer from Merck following the Manufacturer's instructions and 50µg protein per
723 sample was used for further processing. Samples were mixed with 100mM Dithiothreitol (DTT)
724 to get the final concentration of DTT 5mM followed by incubation at 37°C for 1 h at 600rpm in a
725 thermo mixer (Eppendorf). Samples were alkylated with 40mM Chloroacetamide (CAA) and
726 incubated for 30 min at room temperature in the dark. Samples were then mixed with
727 endoproteinase Lys-C (1:75 (w/w) ratio of proteinase to protein) and incubated at 37°C for 4 h.
728 Urea concentration was diluted from 8M to 2M by adding of 50mM TEAB. Samples were
729 incubated with trypsin (1:75 (w/w) ratio of trypsin to protein) overnight at 37°C. Samples were
730 collected and acidified to a final concentration of 1% TFA followed by StageTip extraction. SDB-
731 RP Stage tips were pre-wetted with 30µL 100% MeOH and cleaned with 0.1% TFA, 80% ACN
732 before equilibration with 0.1% TFA. The peptide containing samples were loaded onto SDB-RP
733 StageTip columns and washed once with 30µL 0.1% TFA and twice with 0.1% TFA, 80% ACN
734 followed by drying of StageTips completely with a syringe and stored at 4°C. Prior to
735 measurement StageTips were eluted with 30 µl 1% ammonium hydroxide in 60% ACN, dried in
736 a vacuum concentrator and resuspended in 10 µl 5% FA in 2% ACN. Samples were analysed on a
737 Q-Exactive Plus (Thermo Scientific) mass spectrometer that was coupled to an EASY nLC 1000
738 UPLC (Thermo Scientific). 3 µl resuspended peptides were loaded onto an in-house packed
739 analytical column (50 cm × 75 µm I.D., filled with 2.7 µm Poroshell EC120 C18, Agilent) and
740 equilibrated in solvent A (0.1% FA). Peptides were chromatographically separated at a constant
741 flow rate of 250 nL/min using the following gradient: 5-30% solvent B (0.1% formic acid in 80%
742 acetonitrile) within 65 min, 30-50% solvent B within 13 min, followed by washing and column

743 equilibration. The mass spectrometer was operated in data-dependent acquisition mode. The MS1
744 survey scan was acquired from 300-1750 m/z at a resolution of 70,000. The top 10 most abundant
745 peptides were isolated within a 2 Da window and subjected to HCD fragmentation at a normalized
746 collision energy of 27%. The AGC target was set to 5e5 charges, allowing a maximum injection
747 time of 110 ms. Product ions were detected in the Orbitrap at a resolution of 17,500. Precursors
748 were dynamically excluded for 20 s. Mass spectrometry and bioinformatic data analysis were
749 performed by the CECAD Proteomics facility.

750

751 *Bioinformatic MS data analysis.* All mass spectrometric raw data were processed with Maxquant
752 (version 1.5.3.8) using default parameters (Tyanova et al., 2016). Briefly, MS2 spectra were
753 searched against the Uniprot MOUSE.fasta database, including a list of common contaminants.
754 False discovery rates on protein and PSM level were estimated by the target-decoy approach to
755 0.01% (Protein FDR) and 0.01% (PSM FDR), respectively. The minimal peptide length was set to
756 7 amino acids and carbamidomethylation at cysteine residues was considered as a fixed
757 modification. Oxidation (M) and Acetyl (Protein N-term) were included as variable modifications.
758 The match-between runs option was enabled. LFQ quantification was enabled using default
759 settings. The Maxquant output was processed as follows: Protein groups flagged as „reverse“,
760 „potential contaminant“ or „only identified by site“ were removed from the proteinGroups.txt.
761 LFQ values were log2 transformed. Proteins with less than 3 valid values in at least one group of
762 4 replicates were removed. Missing values were replaced by imputation from a normal distribution
763 (width 0.3, down shift 1.8). Sample t-test was used to determine significantly changing protein
764 levels (q-value <0.05, S0 = 0.2) and a permutation-based FDR was calculated to correct for
765 multiple testing. Enrichment of Gene Ontology, KEGG and GSEA was assessed using 1D
766 annotation enrichment. Moreover, the obtained data was uploaded into the Ingenuity Pathway
767 Analysis (IPA) software (Qiagen) to identify canonical pathways and gene networks that are
768 significantly changed.

769

770 *C₁₃-incorporation measurements.* For U-¹³C₆ glucose (Cambridge Isotope Laboratories, CLM-
771 1396) and U-¹³C₁₆ palmitate (Cambridge Isotope Laboratories, CLM-409) chase, NSPCs were
772 seeded in T25 flask in proliferating media containing normal (¹²C) Glucose (25mM). After 48 h
773 unlabelled proliferating media was replaced with 25 mM U-¹³C₆-labelled glucose or 170 µM U-

774 $^{13}\text{C}_{16}$ -labelled Palmitate media and incubated for 30 min. Cells were washed twice and harvested
775 in ice cold saline. Cell were spin down at 2500 rpm for 5 min at 4°C and pellets were stored at -
776 80°C until further use.

777

778 Whole-cell total metabolite analysis. NSPCs were seeded in T25 flask pre-coated with Poly-D-
779 lysine and Laminin in proliferation media (supplemented with 5x dNTP mix, 20 mM sodium
780 acetate or 150 μM L-Aspartic acid when indicated). After 48 h cells were washed twice and
781 harvested in ice cold saline. Cell were spin down at 2500 rpm for 5 min at 4°C and pellets were
782 stored at -80°C until further use.

783

784 Metabolite extraction for Liquid Chromatography mass spectrometry (LC-MS)

785 Metabolite extraction from each cell pellet was performed using 1 mL of a mixture of 40:40:20
786 [v:v:v] of pre-chilled (-20°C) acetonitrile:methanol:water (OptimaTM LC/MS grade, Fisher
787 Scientific). The samples were subsequently vortexed until the cell pellets were fully suspended,
788 before incubating them on an orbital mixer at 4°C for 30 min at 1500 rpm. For further
789 disintegration, samples were sonicated for 10 min in an ice cooled bath-type sonicator (VWR,
790 Germany) before centrifuging them for 10 min at 21100x g and 4°C. The metabolite-containing
791 supernatant was collected in fresh tubes and concentrated to dryness in a Speed Vac concentrator
792 (Eppendorf). The protein-containing pellets were collected and used for protein quantification
793 (BCA Protein Assay Kit, Thermo Fisher Scientific).

794

795 LC-MS analysis of isotope-enrichments in amino acids after ^{13}C -glucose or ^{13}C palmitate feeding

796 For amino acid analysis a benzoylchlorid derivatization method (Wong et al., 2016) was used. In
797 brief: The dried metabolite pellets was re-suspended in 20 μl LC-MS-grade waters (OptimaTM
798 LC/MS grade, Fisher Scientific). The re-suspended sample were vortexed and 10 μl of 100 mM
799 sodium carbonate (Sigma), followed by 10 μl 2% benzoylchloride (Sigma) in acetonitrile (Optima-
800 Grade, Fisher-Scientific) were added. Samples were well vortexed before centrifuging them for 10
801 min 21.300x g at 20°C. Clear supernatants were transferred to fresh auto sampler tubes with
802 conical glass inserts (Chromatographie Zubehoer Trott) and analyzed using an Acquity iClass
803 UPLC (Waters) connected to a Q-Exactive HF (Thermo) mass spectrometer (MS). For the analysis
804 of the amino acids 1 μL of the derivatized samples was injected onto a 100 x 1.0 mm HSS T3

805 UPLC column (Waters). The flow rate was set to 100 μ L/min using a buffer system consisted of
806 buffer A (10 mM ammonium formate (Sigma), 0.15% formic acid (Sigma) in LC-MS-grade water
807 (OptimaTM LC/MS grade, Fisher Scientific) and buffer B (acetonitrile, Optima-grade, Fisher-
808 Scientific). The LC gradient was: 0% B at 0 min; 0-15% B 0-0.1 min; 15-17% B 0.1-0.5 min; 17-
809 55% B 0.5-14 min, 55-70% B 14-14.5 min; 70-100% B 14.5-18 min; 100% B 18-19 min; 100-0%
810 B 19-19.1 min, 19.1-28 min 0% B. The mass spectrometer was operating in positive ionization
811 mode monitoring a m/z range between 50 and 750. The heated electrospray ionization (ESI) source
812 settings of the mass spectrometer were: Spray voltage 3.5kV, capillary temperature 250°C, sheath
813 gas flow 60 AU and aux gas flow 20 AU at a temperature of 250°C. The S-lens was set to a value
814 of 60 AU. Data analysis of isotope ratios was performed using the TraceFinder software (Version
815 4.2, Thermo Fisher Scientific). Identity of each compound was validated by authentic reference
816 compounds, which were analysed independently. For the isotope enrichment analysis the area of
817 the extracted ion chromatogram (XIC) of each isotope $[M + H]^+$ was determined with a mass
818 accuracy (<5 ppm) and a retention time (RT) precision (<0.1 min), before calculating the
819 proportions of each detected isotope towards the sum of all isotopes of the corresponding
820 compound. These proportions were given as percent values for each isotope.

821

822 *GC-MS analysis of isotope-enrichments in metabolites from glycolysis and TCA cycle after ¹³C-*
823 *glucose or ¹³C palmitate feeding*

824 Similar to the analysis of the isotope enrichment analysis in the amino acids, isotope enrichment
825 analysis of glycolysis and TCA cycle metabolites were determined using gas chromatography
826 (GC) coupled to a high resolution, accurate mass MS (Q-Exactive GC-Orbitrap, Thermo Fisher
827 Scientific). For this analysis metabolites were derivatized using a two-step procedure starting with
828 an methoxyamination (methoxyamine hydrochlorid, Sigma) followed by a trimethyl-silylation
829 using N-Methyl-N-trimethylsilyl-trifluoracetamid (MSTFA, Macherey-Nagel). Dried samples
830 were re-suspended in 5 μ L of a freshly prepared (20 mg/mL) solution of methoxyamine in pyridine
831 (Sigma) to perform the methoxyamination. These samples were then incubated for 90 min at 40°C
832 on an orbital shaker (VWR) at 1500 rpm. In the second step additional 45 μ L of MSTFA were
833 added and the samples were incubated for additional 30 min at 40°C and 1500 rpm. At the end of
834 the derivatisation the samples were centrifuged for 10 min at 21.100x g and 40 μ L of the clear
835 supernatant were transferred to fresh auto sampler vials with conical glass inserts

836 (Chromatographie Zubehör Trott). For the GC-MS analysis 1 μ L of each sample was injected
837 using a PAL autosampler system (Thermo Fisher Scientific) using a Split/Splitless (SSL) injector
838 at 300 °C in splitless-mode. The carrier gas flow (helium) was set to 2 ml/min using a 30m DB-
839 35MS capillary column (0.250 mm diameter and 0.25 μ m film thickness, Agilent). The GC
840 temperature program was: 2 min at 85°C, followed by a 15°C per min ramp to 330°C. At the end
841 of the gradient the temperature was held for additional 6 min at 330°C. The transfer line and source
842 temperature were both set to 280°C. The filament, which was operating at 70 eV, was switched on
843 2 min after the sample was injected. During the whole gradient period the MS was operated in full
844 scan mode covering a m/z range between 70 and 800 with a scan speed of 20 Hertz. For data
845 analysis peak areas of XICs of each isotope of a compound-specific fragment $[M - e^-]^+$ were
846 determined using the TraceFinder software (Version 4.2, Thermo Fisher Scientific). XICs were
847 extracted with a mass accuracy (<5 ppm) and a RT precision (<0.05 min), as compared to
848 independently analysed authentic reference compounds. Subsequently proportions of each
849 detected isotope towards the sum of all isotopes of the corresponding compound-specific fragment
850 were determined. These proportions are given as percent values for each isotope. The flux into
851 each compound was analysed from a single compound-specific fragment. Accordingly, 3-
852 phosphoglyceric acid was analysed from a three carbon-containing fragment with the chemical
853 formula C14H36O7PSi4 and m/z 459.12702. Phosphoenolpyruvic acid was analysed from a three
854 carbon-containing fragment with the chemical formula C11H26O6PSi3 and m/z 369.07693.
855 Pyruvic acid was analysed from a three carbon-containing fragment with the chemical formula
856 C6H12NO3Si and m/z 174.05809. Lactic acid was analysed from a three carbon-containing
857 fragment with the chemical formula C8H19O3Si2 and m/z 219.08672. Citric acid was analysed
858 from a five carbon-containing fragment with the chemical formula C11H21O4Si2 and m/z
859 273.09729. Alpha-ketoglutaric acid was analysed from a five carbon-containing fragment with the
860 chemical formula C8H12NO3Si and m/z 198.058096. Succinic acid was analysed from a four
861 carbon-containing fragment with the chemical formula C9H19O4Si2 and m/z 247.08164. Fumaric
862 acid was analysed from a four carbon-containing fragment with the chemical formula
863 C9H17O4Si2 and m/z of 247.08164. Malic acid was analysed from a four carbon-containing
864 fragment with the chemical formula C9H17O4Si2 and m/z of 247.08164.

865

866 Anion-Exchange Chromatography Mass Spectrometry (AEX-MS) of the analysis of Nucleotides

867 For the analysis and quantification of xy, the dried pellet of the metabolite extract was re-
868 suspended in 100 μ L of H₂O (LC-MS Optima-Grade, Thermo Scientific) and analysed using a
869 Dionex ionchromatogrypy system (ICS 5000, Thermo Scientific). The applied protocol was
870 adopted from (Schwaiger et al., 2017). In brief: 10 μ L of polar metabolite extract were injected in
871 full loop mode using an overfill factor of 3, onto a Dionex IonPac AS11-HC column (2 mm \times 250
872 mm, 4 μ m particle size, Thermo Scientific) equipped with a Dionex IonPac AG11-HC guard
873 column (2 mm \times 50 mm, 4 μ m, Thermo Scientific). The column temperature was held at 30°C,
874 while the auto sampler was set tot 6°C. A potassium hydroxide gradient was generated by the
875 eluent generator using a potassium hydroxide cartridge that was supplied with deionized water.
876 The metabolite separation was carried at a flow rate of 380 μ L/min, applying the following
877 gradient. 0-3 min, 10 mM KOH; 3-12 min, 10–50 mM KOH; 12-19 min, 50-100 mM KOH, 19-
878 21 min, 100 mM KOH, 21-22 min, 100-10 mM KOH. The column was re-equilibrated at 10 mM
879 for 8 min. The eluting metabolites were detected in negative ion mode using ESI MRM (multi
880 reaction monitoring) on a Xevo TQ (Waters) triple quadrupole mass spectrometer applying the
881 following settings: capillary voltage 2.75 kV, desolvation temp. 550°C, desolvation gas flow 800
882 L/h, collision cell gas flow 0.15 mL/min. All peaks were validated using two MRM transitions one
883 for quantification of the compound, while the second ion was used for qualification of the identity
884 of the compound. Data analysis and peak integrationand quantification was performed using the
885 TargetLynx Software (Waters).

886
887 NAD/NADH measurement. NSPCs (2 x 10⁶) were harvested in cold PBS. Cells were spin down at
888 2000 rpm for 5 min at 4 °C and cell pellets were collected for NAD and NADH measurements by
889 using an NAD/NADH colorimetric Assay Kit (Abcam) according to the manufacturer's
890 instructions.

891
892 RNA sequencing
893 NSPCs were harvested in TRIzol reagent (Invitrogen) and RNA was isolated according to the
894 manufacturer's instructions. Libraries were prepared using the Illumina® Stranded TruSeq® RNA
895 sample preparation Kit. Library preparation started with 2 μ g total RNA. ERCC RNA Spike-In
896 Mix that provides a set of external RNA controls was added to the total RNA prior to library
897 preparation to enable performance assessment. After poly-A selection (using poly-T oligo-attached

898 magnetic beads), mRNA was purified and fragmented using divalent cations under elevated
899 temperature. The RNA fragments underwent reverse transcription using random primers. This was
900 followed by second strand cDNA synthesis with DNA Polymerase I and RNase H. After end repair
901 and A-tailing, indexing adapters were ligated. The products were then purified and amplified (14
902 PCR cycles) to create the final cDNA libraries. After library validation and quantification (Tape
903 Station 4200), equimolar amounts of library were pooled. The pool was quantified by using the
904 Peqlab KAPA Library Quantification Kit and the Applied Biosystems 7900HT Sequence
905 Detection System. The pool was sequenced Illumina NovaSeq6000 sequencing instrument with a
906 PE100 protocol.

907

908 **Bioinformatic RNA-Seq data analysis.** Quality control, trimming, and alignment of raw data were
909 performed using the “nf-core” RNA-seq pipeline (v3.0) (Ewels et al., 2020). The reference genome
910 sequence and transcript annotation used were Mus Musculus GRCm39 ensembl v103. Differential
911 expression analysis was performed in R (v4.0.3) (<https://www.R-project.org/>) with “DESeq2”
912 package (v1.30.1) (Love et al., 2014) and Log (Fold Change) shrinkage estimation was calculated
913 with “apeglm” (v1.12.0) (Zhu et al., 2019). Only genes with a minimum coverage of 10 reads in 6
914 or more samples from each pairwise comparison were considered as candidates for differential
915 expression analysis. Genes were considered differentially expressed if they showed a
916 $|log_2(Fold\ Change)| > 0.5$ and if they were below the p-value threshold. Nominally significant p-
917 values were considered with a p-value < 0.05 without multiple testing correction. Expression level
918 data for heatmaps are in length Scaled TPM (Transcripts Per Kilobase Million) units.

919

920 **Quantification and statistical analysis**

921 Data are represented as means \pm SE. Graphical illustrations and significance were obtained with
922 GraphPad Prism 7 (GraphPad). Significance was calculated as described in each figure legend.

923

924

925

926

927

928

REAGENT OR RESOURCE	SOURCE	IDENTIFIER
Antibodies		
Rabbit polyclonal anti-Ki67	Abcam	Cat# ab15580; RRID: AB_443209
Mouse monoclonal anti-Sox2	Abcam	Cat# ab171380; RRID: AB_2732072
Chick polyclonal anti-GFP	Aves Labs	Cat# GFP-1020; RRID: AB_10000240
Mouse monoclonal anti-GFAP, clone GA5	Millipore	Cat# MAB360; RRID: AB_11212597
Rabbit polyclonal anti-GFAP	Millipore	Cat# AB5804; RRID: AB_2109645
Guinea Pig polyclonal anti-NeuN	Millipore	Cat# ABN90P; RRID: AB_2341095
Mouse monoclonal anti-Nestin, clone rat-401	Millipore	Cat# MAB353; RRID: AB_94911
Rabbit polyclonal anti-YME1L	Proteintech	Cat# 11510-1-AP; RRID: AB_2217459
Mouse monoclonal anti-OPA1	BD	Cat# 612607; RRID: AB_399889
Mouse monoclonal anti-PRELID1, clone7B4	Abnova	Cat# H00027166-M01; RRID: AB_534999
Rabbit polyclonal anti-TIMM17A	Gene Tex	Cat# GTX108280; RRID: AB_2038123

Rabbit polyclonal anti-TOMM20 (FL-145)	Santa Cruz	Cat# sc-11415; RRID: AB_2207533
Goat polyclonal anti-doublecortin (C-18)	Santa Cruz	Cat# sc-8066; RRID: AB_2088494
Guinea Pig polyclonal anti-beta3-tubulin	Synaptic System	Cat# 302 304; RRID: AB_10805138
Mouse monoclonal anti-SDHA	Thermo Fisher Scientific	Cat# 459200; RRID: AB_2532231
Mouse polyclonal anti-TBR2	Abcam	Cat# ab23345; RRID: AB_778267
4',6-Diamidino-2-Phenylindole, Dihydrochloride (DAPI)	Thermo Fisher Scientific	Cat# D1306; RRID: AB_2629482
Click-iT EdU imaging Kit (555)	Thermo Fisher Scientific	Cat# C10338
Click-iT EdU imaging Kit (647)	Thermo Fisher Scientific	Cat# C10340
Donkey anti-chicken IgY (H+L), Alexa Fluor 488	Jackson ImmunoResearch	Cat# 703-545-155; RRID: AB_2340375
Donkey anti-Rabbit IgG (H+L), Alexa Fluor 546	Thermo Fisher Scientific	Cat# A10040; RRID: AB_2534016
Donkey anti-Rat IgG (H+L), Alexa Fluor 647	Jackson ImmunoResearch	Cat# 712-605-150; RRID: AB_2340693
Donkey anti-Goat IgG (H+L), Alexa Fluor 488	Jackson ImmunoResearch	Cat# 705-546-147; RRID: AB_2340430

Donkey anti-Guinea Pig IgG (H+L) Alexa Fluor 647	Jackson ImmunoResearch	Cat# 706-605-148; RRID: AB_2340476
Donkey anti-Mouse IgG (H+L) Alexa Fluor 647	Jackson ImmunoResearch	Cat# 715-605-150; RRID: AB_2340862
Donkey anti-Mouse IgG (H+L) Alexa Fluor 546	Thermo Fisher Scientific	Cat# A10036; RRID: AB_2534012
Chemicals, Peptides, and Recombinant Proteins		
Tamoxifen	Sigma-Aldrich	Cat# T5648, CAS: 10540-29-1
Corn-oil	Sigma-Aldrich	Cat# C8267, CAS: 8001-30-7
Paraformaldehyde	Sigma-Aldrich	Cat# P6148, CAS: 30525-89-4
Antimycin A	Santa Cruz	Cat# sc-202467, CAS: 1397-94-0
Oligomycin A	Santa Cruz	Cat# sc-201551, CAS: 579-13-5
Rotenone	Santa Cruz	Cat# sc-203242, CAS: 83-79-4
FCCP	Santa Cruz	Cat# sc-203578, CAS: 370-86-5
B27	Thermo Fisher Scientific	Cat# 17504-044
EGF Mouse	Sigma-Aldrich	Cat# SRP3196
FGF-2 Mouse	Sigma-Aldrich	Cat# SRP4038
Mouse BMP4	R & D Systems	Cat# 5020-BP-010
Laminin	Sigma-Aldrich	Cat# L2020, CAS: 114956-81-9
DNase	Sigma-Aldrich	Cat# 10104159001
Sodium acetate	Sigma-Aldrich	Cat# S2889, CAS: 127-09-3

L-Aspartic acid	Sigma-Aldrich	Cat# A7219, CAS: 56-84-8
dNTP mix	Sigma-Aldrich	Cat# R1121
U- ¹³ C ₁₆ palmitate	Cambridge Isotope Laboratories Inc	Cat# CLM-2241
U- ¹³ C ₆ D-Glucose	Cambridge Isotope Laboratories Inc	Cat# CLM-1396
Seahorse XF96 FluxPak	Agilent	Cat# 102416-100
Seahorse XF Palmitate-BSA FAO Substrate	Agilent	Cat# 102720-100
Bacterial and Virus Strains		
AAV5.CMV.PI.eGFP.WPRE.bG H	Addgene	Cat# 105530-AAV5
AAV5.CMV.HI.eGFP-Cre.WPRE.SV40	Addgene	Cat# 105545-AAV5
AAV1-CAG-hYME1L.WPRE.SV40	This paper	N/A
AAV1-CAG-hYME1L (E543Q).WPRE.SV40	This paper	N/A
Deposited Data		
Raw and analysed Mass Spectrometry Data	This paper	N/A
Raw and analysed Metabolomics Data	This paper	N/A
Raw and analysed RNA-Seq Data	This paper	N/A
Experimental Models: Cell Lines		
Mouse: primary NSPCs wild-type, Yme1 ^{lloxP} , Oma1 ^{lloxP} , Yme1 ^{lloxP} /Oma1 ^{lloxP} , Mfn1 ^{lloxP} and Mfn2 ^{lloxP}	This paper	N/A
Experimental Models: Organisms/Strains		
Mouse: Yme1 ^{lloxP}	Anand et al., 2014	N/A
Mouse: Oma1 ^{lloxP}	Anand et al., 2014	N/A

Mouse: Yme1 ^{loxP} /Oma1 ^{loxP}	Anand et al., 2014	N/A
Mouse: Mfn1 ^{loxP}	Lee et al., 2012	N/A
Mouse: Mfn2 ^{loxP}	Lee et al., 2012	N/A
Mouse: hGFAP-Cre ^{ER}	Chow et al., 2008	N/A
Mouse: Nestin-Cre ^{ERT2}	Lagace et al., 2007	N/A
Mouse: Gt(ROSA26)SorStop-mito-YFP	Sterky et al., 2011	N/A
Mouse: Gt(ROSA26)SorStop-tdTomato	Madisen et al., 2010	N/A
Software and Algorithms		
ImageJ	NIH	http://imagej.nih.gov/ij/ ; RRID: SCR_003070
Fiji	Max-Planck-Gesellschaft	http://fiji.sc ; RRID: SCR_002285
Photoshop CC2017	Adobe	https://www.adobe.com/
Ingenuity Pathway Analysis (IPA)	Qiagen	http://www.ingenuity.com/products/pathways_analysis.html ; RRID: SCR_008653
GraphPad Prism 7.0	GraphPad Software	https://www.graphpad.com/scientific-software/prism ; RRID: SCR_002798
Huygens Professional	Scientific Volume Imaging	RRID: SCR_014237
Adobe Illustrator CS6	Adobe	RRID: SCR_014198

929

930

931

932 **References**

933 Adusumilli, V.S., Walker, T.L., Overall, R.W., Klatt, G.M., Zeidan, S.A., Zocher, S., Kirova,
934 D.G., Ntitsias, K., Fischer, T.J., Sykes, A.M., Reinhardt, S., Dahl, A., Mansfeld, J., Runker, A.E.,
935 and Kempermann, G. (2021). ROS Dynamics Delineate Functional States of Hippocampal Neural
936 Stem Cells and Link to Their Activity-Dependent Exit from Quiescence. *Cell stem cell* 28, 300-
937 314 e306.

938 Ahlqvist, K.J., Hamalainen, R.H., Yatsuga, S., Uutela, M., Terzioglu, M., Gotz, A., Forsstrom, S.,
939 Salven, P., Angers-Loustau, A., Kopra, O.H., Tyynismaa, H., Larsson, N.G., Wartiovaara, K.,
940 Prolla, T., Trifunovic, A., and Suomalainen, A. (2012). Somatic progenitor cell vulnerability to
941 mitochondrial DNA mutagenesis underlies progeroid phenotypes in Polg mutator mice. *Cell
942 Metab* 15, 100-109.

943 Anand, R., Wai, T., Baker, M.J., Kladt, N., Schauss, A.C., Rugarli, E., and Langer, T. (2014). The
944 i-AAA protease YME1L and OMA1 cleave OPA1 to balance mitochondrial fusion and fission. *J
945 Cell Biol* 204, 919-929.

946 Beckervordersandforth, R., Ebert, B., Schaffner, I., Moss, J., Fiebig, C., Shin, J., Moore, D.L.,
947 Ghosh, L., Trincheri, M.F., Stockburger, C., Friedland, K., Steib, K., von Wittgenstein, J., Keiner,
948 S., Redecker, C., Holter, S.M., Xiang, W., Wurst, W., Jagasia, R., Schinder, A.F., Ming, G.L.,
949 Toni, N., Jessberger, S., Song, H., and Lie, D.C. (2017). Role of Mitochondrial Metabolism in the
950 Control of Early Lineage Progression and Aging Phenotypes in Adult Hippocampal Neurogenesis.
951 *Neuron* 93, 560-573 e566.

952 Bonaguidi, M.A., Wheeler, M.A., Shapiro, J.S., Stadel, R.P., Sun, G.J., Ming, G.L., and Song, H.
953 (2011). In vivo clonal analysis reveals self-renewing and multipotent adult neural stem cell
954 characteristics. *Cell* 145, 1142-1155.

955 Bottes, S., Jaeger, B.N., Pilz, G.A., Jorg, D.J., Cole, J.D., Kruse, M., Harris, L., Korobeynyk, V.I.,
956 Mallona, I., Helmchen, F., Guillemot, F., Simons, B.D., and Jessberger, S. (2021). Long-term self-
957 renewing stem cells in the adult mouse hippocampus identified by intravital imaging. *Nat Neurosci*
958 24, 225-233.

959 Brunner, A.-D., Thielert, M., Vasilopoulou, C.G., Ammar, C., Coscia, F., Mund, A., Hoerning,
960 O.B., Bache, N., Apalategui, A., Lubeck, M., Richter, S., Fischer, D.S., Raether, O., Park, M.A.,

961 Meier, F., Theis, F.J., and Mann, M. (2021). Ultra-high sensitivity mass spectrometry quantifies
962 single-cell proteome changes upon perturbation. *bioRxiv*.

963 Chow, L.M., Zhang, J., and Baker, S.J. (2008). Inducible Cre recombinase activity in mouse
964 mature astrocytes and adult neural precursor cells. *Transgenic research* 17, 919-928.

965 Deshwal, S., Fiedler, K.U., and Langer, T. (2020). Mitochondrial Proteases: Multifaceted
966 Regulators of Mitochondrial Plasticity. *Annu Rev Biochem* 89, 501-528.

967 Encinas, J.M., Michurina, T.V., Peunova, N., Park, J.H., Tordo, J., Peterson, D.A., Fishell, G.,
968 Koulakov, A., and Enikolopov, G. (2011). Division-coupled astrocytic differentiation and age-
969 related depletion of neural stem cells in the adult hippocampus. *Cell stem cell* 8, 566-579.

970 Ewels, P.A., Peltzer, A., Fillinger, S., Patel, H., Alneberg, J., Wilm, A., Garcia, M.U., Di
971 Tommaso, P., and Nahnse, S. (2020). The nf-core framework for community-curated
972 bioinformatics pipelines. *Nature biotechnology* 38, 276-278.

973 Göbel, J., Engelhardt, E., Pelzer, P., Sakthivelu, V., Jahn, H.M., Jevtic, M., Folz-Donahue, K.,
974 Kukat, C., Schauss, A., Frese, C.K., Giavalisco, P., Ghanem, A., Conzelmann, K.K., Motori, E.,
975 and Bergami, M. (2020). Mitochondria-Endoplasmic Reticulum Contacts in Reactive Astrocytes
976 Promote Vascular Remodeling. *Cell Metab* 31, 791-808 e798.

977 Goncalves, J.T., Schafer, S.T., and Gage, F.H. (2016). Adult Neurogenesis in the Hippocampus:
978 From Stem Cells to Behavior. *Cell* 167, 897-914.

979 Griparic, L., Kanazawa, T., and van der Bliek, A.M. (2007). Regulation of the mitochondrial
980 dynamin-like protein Opal by proteolytic cleavage. *J Cell Biol* 178, 757-764.

981 Guo, W., Patzlaff, N.E., Jobe, E.M., and Zhao, X. (2012). Isolation of multipotent neural stem or
982 progenitor cells from both the dentate gyrus and subventricular zone of a single adult mouse.
983 *Nature protocols* 7, 2005-2012.

984 Harris, L., Rigo, P., Stiehl, T., Gaber, Z.B., Austin, S.H.L., Masdeu, M.D.M., Edwards, A., Urban,
985 N., Marciniak-Czochra, A., and Guillemot, F. (2021). Coordinated changes in cellular behavior
986 ensure the lifelong maintenance of the hippocampal stem cell population. *Cell stem cell* 28, 863-
987 876 e866.

988 Hartmann, B., Wai, T., Hu, H., MacVicar, T., Musante, L., Fischer-Zirnsak, B., Stenzel, W., Graf,
989 R., van den Heuvel, L., Ropers, H.H., Wienker, T.F., Hubner, C., Langer, T., and Kaindl, A.M.

990 (2016). Homozygous YME1L1 mutation causes mitochondrialopathy with optic atrophy and
991 mitochondrial network fragmentation. *eLife* 5.

992 Homem, C.C., Steinmann, V., Burkard, T.R., Jais, A., Esterbauer, H., and Knoblich, J.A. (2014).
993 Ecdysone and mediator change energy metabolism to terminate proliferation in *Drosophila* neural
994 stem cells. *Cell* 158, 874-888.

995 Ibrayeva, A., Bay, M., Pu, E., Jorg, D.J., Peng, L., Jun, H., Zhang, N., Aaron, D., Lin, C., Resler,
996 G., Hidalgo, A., Jang, M.H., Simons, B.D., and Bonaguidi, M.A. (2021). Early stem cell aging in
997 the mature brain. *Cell stem cell* 28, 955-966 e957.

998 Iwata, R., Casimir, P., and Vanderhaeghen, P. (2020). Mitochondrial dynamics in postmitotic cells
999 regulate neurogenesis. *Science* 369, 858-862.

1000 Khacho, M., Clark, A., Svoboda, D.S., Azzi, J., MacLaurin, J.G., Meghaizel, C., Sesaki, H.,
1001 Lagace, D.C., Germain, M., Harper, M.E., Park, D.S., and Slack, R.S. (2016). Mitochondrial
1002 Dynamics Impacts Stem Cell Identity and Fate Decisions by Regulating a Nuclear Transcriptional
1003 Program. *Cell stem cell* 19, 232-247.

1004 Knobloch, M., Braun, S.M., Zurkirchen, L., von Schoultz, C., Zamboni, N., Arauzo-Bravo, M.J.,
1005 Kovacs, W.J., Karalay, O., Suter, U., Machado, R.A., Roccio, M., Lutolf, M.P., Semenkovich,
1006 C.F., and Jessberger, S. (2013). Metabolic control of adult neural stem cell activity by Fasn-
1007 dependent lipogenesis. *Nature* 493, 226-230.

1008 Knobloch, M., Pilz, G.A., Ghesquiere, B., Kovacs, W.J., Wegleiter, T., Moore, D.L., Hruzova, M.,
1009 Zamboni, N., Carmeliet, P., and Jessberger, S. (2017). A Fatty Acid Oxidation-Dependent
1010 Metabolic Shift Regulates Adult Neural Stem Cell Activity. *Cell reports* 20, 2144-2155.

1011 Lagace, D.C., Whitman, M.C., Noonan, M.A., Ables, J.L., DeCarolis, N.A., Arguello, A.A.,
1012 Donovan, M.H., Fischer, S.J., Farnbauch, L.A., Beech, R.D., DiLeone, R.J., Greer, C.A.,
1013 Mandyam, C.D., and Eisch, A.J. (2007). Dynamic contribution of nestin-expressing stem cells to
1014 adult neurogenesis. *J Neurosci* 27, 12623-12629.

1015 Lee, S., Sterky, F.H., Mourier, A., Terzioglu, M., Cullheim, S., Olson, L., and Larsson, N.G.
1016 (2012). Mitofusin 2 is necessary for striatal axonal projections of midbrain dopamine neurons.
1017 *Human molecular genetics* 21, 4827-4835.

1018 Leeman, D.S., Hebestreit, K., Ruetz, T., Webb, A.E., McKay, A., Pollina, E.A., Dulken, B.W.,
1019 Zhao, X., Yeo, R.W., Ho, T.T., Mahmoudi, S., Devarajan, K., Passegue, E., Rando, T.A., Frydman,

1020 J., and Brunet, A. (2018). Lysosome activation clears aggregates and enhances quiescent neural
1021 stem cell activation during aging. *Science* 359, 1277-1283.

1022 Llorens-Bobadilla, E., Zhao, S., Baser, A., Saiz-Castro, G., Zwadlo, K., and Martin-Villalba, A.
1023 (2015). Single-Cell Transcriptomics Reveals a Population of Dormant Neural Stem Cells that
1024 Become Activated upon Brain Injury. *Cell stem cell* 17, 329-340.

1025 Love, M.I., Huber, W., and Anders, S. (2014). Moderated estimation of fold change and dispersion
1026 for RNA-seq data with DESeq2. *Genome biology* 15, 550.

1027 MacVicar, T., Ohba, Y., Nolte, H., Mayer, F.C., Tatsuta, T., Sprenger, H.G., Lindner, B., Zhao,
1028 Y., Li, J., Bruns, C., Kruger, M., Habich, M., Riemer, J., Schwarzer, R., Pasparakis, M., Henschke,
1029 S., Bruning, J.C., Zamboni, N., and Langer, T. (2019). Lipid signalling drives proteolytic rewiring
1030 of mitochondria by YME1L. *Nature* 575, 361-365.

1031 Madisen, L., Zwingman, T.A., Sunkin, S.M., Oh, S.W., Zariwala, H.A., Gu, H., Ng, L.L., Palmiter,
1032 R.D., Hawrylycz, M.J., Jones, A.R., Lein, E.S., and Zeng, H. (2010). A robust and high-throughput
1033 Cre reporting and characterization system for the whole mouse brain. *Nat Neurosci* 13, 133-140.

1034 Mehta, M.M., Weinberg, S.E., and Chandel, N.S. (2017). Mitochondrial control of immunity:
1035 beyond ATP. *Nat Rev Immunol* 17, 608-620.

1036 Mira, H., Andreu, Z., Suh, H., Lie, D.C., Jessberger, S., Consiglio, A., San Emeterio, J.,
1037 Hortiguela, R., Marques-Torrejon, M.A., Nakashima, K., Colak, D., Gotz, M., Farinas, I., and
1038 Gage, F.H. (2010). Signaling through BMPR-IA regulates quiescence and long-term activity of
1039 neural stem cells in the adult hippocampus. *Cell stem cell* 7, 78-89.

1040 Mishra, P., Carelli, V., Manfredi, G., and Chan, D.C. (2014). Proteolytic cleavage of Opa1
1041 stimulates mitochondrial inner membrane fusion and couples fusion to oxidative phosphorylation.
1042 *Cell Metab* 19, 630-641.

1043 Morrow, C.S., Porter, T.J., Xu, N., Arndt, Z.P., Ako-Asare, K., Heo, H.J., Thompson, E.A.N., and
1044 Moore, D.L. (2020). Vimentin Coordinates Protein Turnover at the Aggresome during Neural
1045 Stem Cell Quiescence Exit. *Cell stem cell* 26, 558-568 e559.

1046 Nakamura-Ishizu, A., Ito, K., and Suda, T. (2020). Hematopoietic Stem Cell Metabolism during
1047 Development and Aging. *Dev Cell* 54, 239-255.

1048 Namba, T., Doczi, J., Pinson, A., Xing, L., Kalebic, N., Wilsch-Brauninger, M., Long, K.R., Vaid,
1049 S., Lauer, J., Bogdanova, A., Borgonovo, B., Shevchenko, A., Keller, P., Drechsel, D., Kurzchalia,
1050 T., Wimberger, P., Chinopoulos, C., and Huttner, W.B. (2020). Human-Specific ARHGAP11B

1051 1052 Acts in Mitochondria to Expand Neocortical Progenitors by Glutaminolysis. *Neuron* 105, 867-881
e869.

1053 1054 Navarro Negredo, P., Yeo, R.W., and Brunet, A. (2020). Aging and Rejuvenation of Neural Stem
Cells and Their Niches. *Cell stem cell* 27, 202-223.

1055 1056 1057 Pilz, G.A., Bottes, S., Betizeau, M., Jorg, D.J., Carta, S., Simons, B.D., Helmchen, F., and
Jessberger, S. (2018). Live imaging of neurogenesis in the adult mouse hippocampus. *Science* 359,
658-662.

1058 1059 1060 Prozorovski, T., Schulze-Topphoff, U., Glumm, R., Baumgart, J., Schroter, F., Ninnemann, O.,
Siebert, E., Bendix, I., Brustle, O., Nitsch, R., Zipp, F., and Aktas, O. (2008). Sirt1 contributes
critically to the redox-dependent fate of neural progenitors. *Nat Cell Biol* 10, 385-394.

1061 1062 Puleston, D.J., Villa, M., and Pearce, E.L. (2017). Ancillary Activity: Beyond Core Metabolism
in Immune Cells. *Cell Metab* 26, 131-141.

1063 1064 Quiros, P.M., Langer, T., and Lopez-Otin, C. (2015). New roles for mitochondrial proteases in
health, ageing and disease. *Nat Rev Mol Cell Biol* 16, 345-359.

1065 1066 1067 1068 1069 1070 Rath, S., Sharma, R., Gupta, R., Ast, T., Chan, C., Durham, T.J., Goodman, R.P., Grabarek, Z.,
Haas, M.E., Hung, W.H.W., Joshi, P.R., Jourdain, A.A., Kim, S.H., Kotrys, A.V., Lam, S.S.,
McCoy, J.G., Meisel, J.D., Miranda, M., Panda, A., Patgiri, A., Rogers, R., Sadre, S., Shah, H.,
Skinner, O.S., To, T.L., Walker, M.A., Wang, H., Ward, P.S., Wengrod, J., Yuan, C.C., Calvo,
S.E., and Mootha, V.K. (2021). MitoCarta3.0: an updated mitochondrial proteome now with sub-
organelle localization and pathway annotations. *Nucleic acids research* 49, D1541-D1547.

1071 1072 1073 1074 Schaffner, I., Minakaki, G., Khan, M.A., Balta, E.A., Schlotzer-Schrehardt, U., Schwarz, T.J.,
Beckervordersandforth, R., Winner, B., Webb, A.E., DePinho, R.A., Paik, J., Wurst, W., Klucken,
J., and Lie, D.C. (2018). FoxO Function Is Essential for Maintenance of Autophagic Flux and
Neuronal Morphogenesis in Adult Neurogenesis. *Neuron* 99, 1188-1203 e1186.

1075 1076 1077 Schoors, S., Bruning, U., Missiaen, R., Queiroz, K.C., Borgers, G., Elia, I., Zecchin, A., Cantelmo,
A.R., Christen, S., Goveia, J., Heggermont, W., Godde, L., Vinckier, S., Van Veldhoven, P.P.,
Eelen, G., Schoonjans, L., Gerhardt, H., Dewerchin, M., Baes, M., De Bock, K., Ghesquiere, B.,

1078 Lunt, S.Y., Fendt, S.M., and Carmeliet, P. (2015). Fatty acid carbon is essential for dNTP synthesis
1079 in endothelial cells. *Nature* 520, 192-197.

1080 Schwaiger, M., Rampler, E., Hermann, G., Miklos, W., Berger, W., and Koellensperger, G. (2017).
1081 Anion-Exchange Chromatography Coupled to High-Resolution Mass Spectrometry: A Powerful
1082 Tool for Merging Targeted and Non-targeted Metabolomics. *Anal Chem* 89, 7667-7674.

1083 Shin, J., Berg, D.A., Zhu, Y., Shin, J.Y., Song, J., Bonaguidi, M.A., Enikolopov, G., Nauen, D.W.,
1084 Christian, K.M., Ming, G.L., and Song, H. (2015). Single-Cell RNA-Seq with Waterfall Reveals
1085 Molecular Cascades underlying Adult Neurogenesis. *Cell stem cell* 17, 360-372.

1086 Snaebjornsson, M.T., Janaki-Raman, S., and Schulze, A. (2020). Greasing the Wheels of the
1087 Cancer Machine: The Role of Lipid Metabolism in Cancer. *Cell Metab* 31, 62-76.

1088 Song, Z., Chen, H., Fiket, M., Alexander, C., and Chan, D.C. (2007). OPA1 processing controls
1089 mitochondrial fusion and is regulated by mRNA splicing, membrane potential, and Yme1L. *J Cell
1090 Biol* 178, 749-755.

1091 Sprenger, H.G., MacVicar, T., Bahat, A., Fiedler, K.U., Hermans, S., Ehrentraut, D., Ried, K.,
1092 Milenkovic, D., Bonekamp, N., Larsson, N.G., Nolte, H., Giavalisco, P., and Langer, T. (2021).
1093 Cellular pyrimidine imbalance triggers mitochondrial DNA-dependent innate immunity. *Nature
1094 metabolism* 3, 636-650.

1095 Sprenger, H.G., Wani, G., Hesseling, A., Konig, T., Patron, M., MacVicar, T., Ahola, S., Wai, T.,
1096 Barth, E., Rugarli, E.I., Bergami, M., and Langer, T. (2019). Loss of the mitochondrial i-AAA

1097 protease YME1L leads to ocular dysfunction and spinal axonopathy. EMBO molecular medicine
1098 11.

1099 Sterky, F.H., Lee, S., Wibom, R., Olson, L., and Larsson, N.G. (2011). Impaired mitochondrial
1100 transport and Parkin-independent degeneration of respiratory chain-deficient dopamine neurons in
1101 vivo. Proc Natl Acad Sci U S A 108, 12937-12942.

1102 Stoll, E.A., Makin, R., Sweet, I.R., Trevelyan, A.J., Miwa, S., Horner, P.J., and Turnbull, D.M.
1103 (2015). Neural Stem Cells in the Adult Subventricular Zone Oxidize Fatty Acids to Produce
1104 Energy and Support Neurogenic Activity. Stem Cells 33, 2306-2319.

1105 Tyanova, S., Temu, T., and Cox, J. (2016). The MaxQuant computational platform for mass
1106 spectrometry-based shotgun proteomics. Nature protocols 11, 2301-2319.

1107 Wai, T., Garcia-Prieto, J., Baker, M.J., Merkwirth, C., Benit, P., Rustin, P., Ruperez, F.J., Barbas,
1108 C., Ibanez, B., and Langer, T. (2015). Imbalanced OPA1 processing and mitochondrial
1109 fragmentation cause heart failure in mice. Science 350, aad0116.

1110 Walker, T.L., and Kempermann, G. (2014). One mouse, two cultures: isolation and culture of adult
1111 neural stem cells from the two neurogenic zones of individual mice. Journal of visualized
1112 experiments : JoVE, e51225.

1113 Wong, J.M., Malec, P.A., Mabrouk, O.S., Ro, J., Dus, M., and Kennedy, R.T. (2016). Benzoyl
1114 chloride derivatization with liquid chromatography-mass spectrometry for targeted metabolomics
1115 of neurochemicals in biological samples. J Chromatogr A 1446, 78-90.

1116 Xie, Z., Jones, A., Deeney, J.T., Hur, S.K., and Bankaitis, V.A. (2016). Inborn Errors of Long-
1117 Chain Fatty Acid beta-Oxidation Link Neural Stem Cell Self-Renewal to Autism. Cell reports 14,
1118 991-999.

1119 Zhu, A., Ibrahim, J.G., and Love, M.I. (2019). Heavy-tailed prior distributions for sequence count
1120 data: removing the noise and preserving large differences. Bioinformatics 35, 2084-2092.

1121

1122

1123

1124

1125

1126

1127

1128

1129

1130 **Figure legends**

1131 **Figure 1. NSPC state-dependent regulation of YME1L activity.** **(A)** Experimental setting used
1132 for isolating NSPCs from the adult DG and for their maintenance as either actively proliferating
1133 (aNSPCs) or quiescent cells (qNSPCs) following BMP4 addition. **(B)** EdU labelling of aNSPCs
1134 and qNSPCs and relative quantification (n= 6 and 5 experiments; unpaired t-test). Bar, 80 μ m. **(C)**
1135 IPA pathways most significantly enriched in either aNSPCs (10 most significant) or qNSPCs (10
1136 most significant). Categories selected for having a p value \leq 0.01 and a fold enrichment of at least
1137 0.5. **(D)** Cluster analysis of the mitochondrial proteome in aNSPCs, qNSPCs and ex-qNSPCs,
1138 displayed according to mitochondrial compartment (OMM, outer mitochondrial membrane; IMS,
1139 intermembrane space; IMM, inner mitochondrial membrane). Normalized expression levels are
1140 depicted as heat-maps for each quantified protein and scaled row-wise (n=4 experiments per
1141 condition). The right panel shows the matched distribution of the quantified proteins and enzymes
1142 associated to the indicated pathways. **(E)** Cluster analysis of the transcriptome corresponding to
1143 mitochondrial proteins in aNSPCs and qNSPCs (n=4 experiments per condition; nTPM,
1144 normalized transcripts per million). **(F)** Abundance levels (label-free quantification, LFQ
1145 intensities) of the 5 mitochondrial proteases displaying significant state-dependent changes in
1146 NSPCs (n=4 experiments per condition; non-parametric Kruskal-Wallis test). **(G)** Normalized
1147 changes in mRNA expression levels between qNSPCs and aNSPCs of the 5 mito-proteases shown
1148 in F. **(H)** Immunoblot of wild-type and Yme11^{cKO} NSPCs with or without expression of Yme11^{WT}
1149 or Yme11^{E543Q}, maintained as active or quiescent (data representative from two independent
1150 experiments). **(I)** Z-score heat-maps of normalized LFQ intensities of detected class I putative
1151 YME1L substrates in aNSPCs, qNSPCs and ex-qNSPCs, categorized according to their function.
1152 Significant changes (n=4 experiments per condition; FDR-adjusted \leq 0.05) are indicated with an
1153 asterisk (red asterisk: qNSPCs significant vs both aNSPCs and ex-NSPCs; black asterisk: qNSPCs
1154 significant vs only one other category). **(J)** Fold change of mRNA levels of the indicated genes
1155 between qNSPCs and aNSPCs (n=4 experiments; FDR-adjusted \leq 0.05). Means \pm SEM; *, P
1156 < 0.05 ; **, P < 0.01 ; ***, P < 0.005 ; ns, not significant. See also Figures S1 and S2.

1157

1158 **Figure 2. YME1L-dependent rewiring of the mitochondrial proteome in adult NSPCs.** **(A)**
1159 Heat maps of normalized LFQ intensities of detected class I YME1L putative substrates in control
1160 and Yme11^{cKO} NSPCs. Significant changes are indicated with an asterisk (n= 4 experiments per

1161 condition; FDR-adjusted ≤ 0.05). **(B)** mRNA levels of class I YME1L putative substrates in
1162 Yme1l^{cKO} versus control NSPCs (n= 3 experiments; FDR-adjusted ≤ 0.05). **(C)** Volcano plots
1163 showing the changes in the mitochondrial proteome of quiescent vs active states in control (wild-
1164 type) and Yme1l^{cKO} NSPCs. Cut-off line set at $-\log_{10}$ (P-value) = 1.3 (n= 4 experiments per
1165 dataset). **(D)** Whole-proteome cluster analysis of control and Yme1l^{cKO} NSPCs maintained under
1166 active, quiescent and differentiating conditions. Normalized expression levels are depicted as heat-
1167 maps for each quantified protein and scaled row-wise (n= 4 experiments per condition). **(E)** PCA
1168 plot of control and Yme1l^{cKO} aNSPCs, qNSPCs and dNSPCs proteomic datasets (n= 4 experiments
1169 per condition). **(F)** Abundance levels (LFQ intensities) of selected neuronal (TUBB3, CAMK2A
1170 and MAP2) and astrocytic (CX43, GS and ALDH1L1) markers in control and Yme1l^{cKO} aNSPCs,
1171 qNSPCs and dNSPCs (n= 4 experiments per condition; non-parametric Kruskal-Wallis test). **(G)**
1172 Representative examples of control and Yme1l^{cKO} NSPCs maintained under proliferative media
1173 and immunostained for the neuronal marker β -3 tubulin (TUBB3). Images are presented in
1174 pseudocolors. Insets show location of nuclei. Bar, 50 μ m. **(H)** Quantification of β -3 tubulin
1175 immunoreactivity in control and Yme1l^{cKO} NSPCs maintained under proliferative media (n= 66
1176 and 69 cells pooled from 2 independent experiments; Welch's t-test). **(I)** Experimental timeline
1177 used to induce short NSPC differentiation combined with EdU labeling for the experiment shown
1178 in J. **(J)** Representative examples of control and Yme1l^{cKO} NSPCs exposed for 2 days to
1179 differentiation media and immunostained for the EdU and for the neuronal marker β -3 tubulin.
1180 Bar, 80 μ m. **(K)** Quantification of the experiment shown in J (n= 3 independent experiments;
1181 Welch's t-test). Means \pm SEM; *, P < 0.05; **, P < 0.01; ***, P < 0.005; ns, not significant. See
1182 also Figure S2.

1183

1184 **Figure 3. Impaired FAO in adult NSPCs lacking YME1L.** **(A)** Volcano plot showing the
1185 changes of mitochondrial FAO-associated proteins in Yme1l^{cKO} NSPCs (n= 4 experiments). Cut-
1186 off line set at $-\log_{10}$ (P-value) = 1.3. **(B)** Heat-maps of normalized LFQ intensities of FAO-
1187 associated proteins in control and Yme1l^{cKO} NSPCs maintained in either proliferative or quiescent
1188 conditions (n= 4 experiments per condition). **(C)** mRNA levels of FAO enzymes in Yme1l^{cKO}
1189 versus control NSPCs (n= 3 experiments; FDR-adjusted ≤ 0.05). **(D)** Oxygen consumption rates
1190 of control and Yme1l^{cKO} NSPCs fed with either glucose or palmitate (n= 30 repetitions pooled
1191 from 3 independent experiments; Holm-Sidak multiple t-test). **(E)** SeaHorse analysis of basal

1192 respiration, ATP production, maximal respiration and spare respiratory capacity in *Yme1l*^{cKO}
1193 NSPCs fed with either glucose or palmitate (n= 3 to 5 independent experiments; unpaired t-test).
1194 (F) Examples of NSPCs of the indicated genotype following incubation with
1195 Tetramethylrhodamine methyl ester (TMRM, 25 nM) for 10 minutes. Bar, 10 μ m. (G)
1196 Quantification of TMRM signal intensity in control and *Yme1l*^{cKO} NSPCs (n= 34-36 cells pooled
1197 from 2 independent experiments; Welch's t-test). (H) Electron micrographs of mitochondria in
1198 control and *Yme1l*^{cKO} NSPCs. Bar, 500 nm. Means \pm SEM; *, P < 0.05; **, P < 0.01; ***, P
1199 < 0.005; ns, not significant. See also Figure S3.

1200

1201 **Figure 4. Loss of YME1L in NSPCs impairs fatty-acid carbon feeding into the TCA cycle**
1202 **resulting in dNTP pool depletion.** (A) Quantification of TCA cycle metabolites following either
1203 U-¹³C₆-Glucose or U-¹³C₆-Palmitate isotope labelling in control and *Yme1l*^{cKO} NSPCs (n= 4
1204 experiments per condition; Holm-Sidak multiple t-test). M.P.E., Molar Percent Enrichment
1205 (calculated for each isotope). (B) Quantification of newly-synthetized amino acids following either
1206 U-¹³C₆-Glucose or U-¹³C₆-Palmitate isotope labelling in control and *Yme1l*^{cKO} NSPCs (n= 4
1207 experiments per condition; Holm-Sidak multiple t-test). (C) Quantification of dNTP levels in
1208 control and *Yme1l*^{cKO} NSPCs with or without supplementation with the indicated compounds (n=
1209 n= 4 experiments per condition; Two-way Anova followed by Tukey's multiple comparison test).
1210 (D) Examples showing EdU incorporation in *Yme1l*^{cKO} NSPC cultures with or without
1211 supplementation of exogenous dNTPs, acetate or aspartate. Bar, 80 μ m. (E) Quantification of
1212 NSPC proliferation with or without supplementation of exogenous dNTPs, acetate or aspartate (n=
1213 n= 3 experiments per condition; One-way Anova followed by Holm-Sidak's correction). Means \pm
1214 SEM; *, P < 0.05; **, P < 0.01; ***, P < 0.005; ns, not significant. See also Figure S3.

1215

1216 **Figure 5. Defective NSPC proliferation in the adult DG of *Yme1l*^{cKO} mice.** (A) Experimental
1217 design illustrating the tamoxifen-induced conditional deletion of *Yme1l*, or *Yme1l* and *Oma1*, in
1218 hGFAP::Cre^{ER} x mtYFP^{LSL} mice. (B) Examples of radial glia-like mtYFP⁺/GFAP⁺ NSPCs (see
1219 inset) in the DG of the indicated genotypes, showing the morphology of individual mitochondria.
1220 Arrowheads points to the cell soma. Right panels show zooms of the boxed areas along the main
1221 radial process. Bar, 15 μ m. (C) Examples of EdU labelling in the DG of the indicated genotypes.

1222 Insets show zooms of the boxed areas. Bar, 70 μ m. **(D)** Quantification of NSPC proliferation for
1223 the indicated genotypes (n= 5-10 mice per group; One-way Anova followed by Holm-Sidak's
1224 multiple comparison test). **(E)** Quantification of NSPC proliferation for the indicated genotypes
1225 and conditions following delivery of mock, Yme1l^{E543Q} or Yme1l^{WT} AAVs (n= 3-8 mice per
1226 group; One-way Anova followed by Holm-Sidak's multiple comparison test). **(F)** Experimental
1227 design utilized to assess NSPC proliferation at 10 days after tamoxifen-induced recombination in
1228 Yme1l^{cKO} mice. **(G)** Examples of Nestin, EdU and mtYFP labelling in the DG of the indicated
1229 genotypes. Arrowheads point to EdU⁺ cells. Insets show zooms of individual Nestin⁺/EdU⁺ cells.
1230 Bar, 30 μ m. **(H)** Quantification of Nestin⁺, EdU⁺ and Nestin⁺/EdU⁺ NSPCs in control and
1231 Yme1l^{cKO} mice (n= 4-6 mice per group; Welch's t-test). Means \pm SEM; *, P < 0.05; **, P < 0.01;
1232 ***, P < 0.005; ns, not significant. See also Figures S4 and S5.

1233

1234 **Figure 6. Yme1l conditional deletion promotes NSPC pool depletion at the expenses of self-
1235 renewal.** **(A)** Experimental design illustrating the tamoxifen-induced conditional deletion of
1236 Yme1l in Yme1l^{lox/lox} x Nestin::Cre^{ERT2} x tdTomato^{LSL} mice. **(B)** Examples showing the amount of
1237 tdTomato⁺ cells and Dcx⁺ new neurons by 1 month after tamoxifen administration. Bar, 30 μ m.
1238 **(C)** Quantification of tdTomato⁺ cells according to their identity (SOX2⁺ RGL NSPCs; Dcx⁺
1239 immature neurons; Dcx⁺/NeuN⁺ maturing neurons; and NeuN⁺ mature neurons) at 4 and 12 weeks
1240 after tamoxifen-mediated recombination (n= 3-4 mice per group; Holm-Sidak multiple t-test). **(D)**
1241 Percentage of tdTomato⁺ immature and mature neurons at 4 and 12 weeks post-recombination
1242 quantified according to C (n= 3-4 mice per group; Holm-Sidak multiple t-test). **(E)** Examples of
1243 individual clones at 1 month after tamoxifen administration. The putative lineage outcome of each
1244 initially recombined radial glia-like NSPC (R) is shown. Bars, 25 μ m. **(F)** Fraction of clones
1245 containing (with R) or depleted of (without R) radial glia-like NSPCs for the indicated genotypes
1246 (n= 7-8 mice per group). **(G)** Quantification of clones containing single R (quiescent), R+X (self-
1247 renewing) and no R (depleted) for the indicated genotypes (n= 7-8 mice per group, Two-way
1248 Anova followed by Tukey's multiple comparison test). **(H)** Proportion of R-containing clones
1249 classified according to their cellular composition (n= 7-8 mice per group, Two-way Anova
1250 followed by Tukey's multiple comparison test) (R, radial glia-like NSPC; N, neuron; A, astrocyte).
1251 Inset reports on the number of Rs per clone (n= 7-8 animals per group). Means \pm SEM; *, P < 0.05;
1252 **, P < 0.01; ***, P < 0.005; ns, not significant. See also Figure S6.

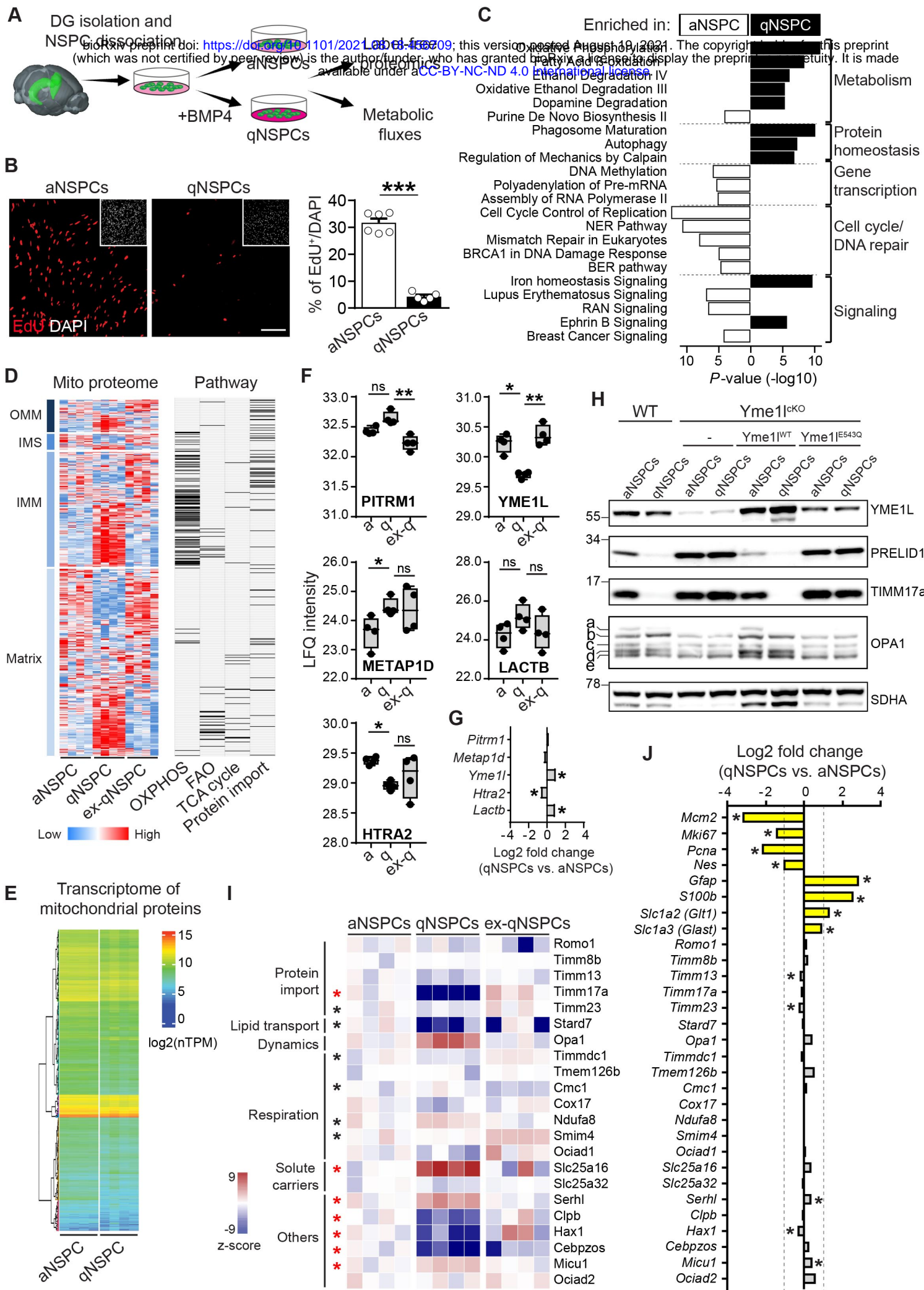
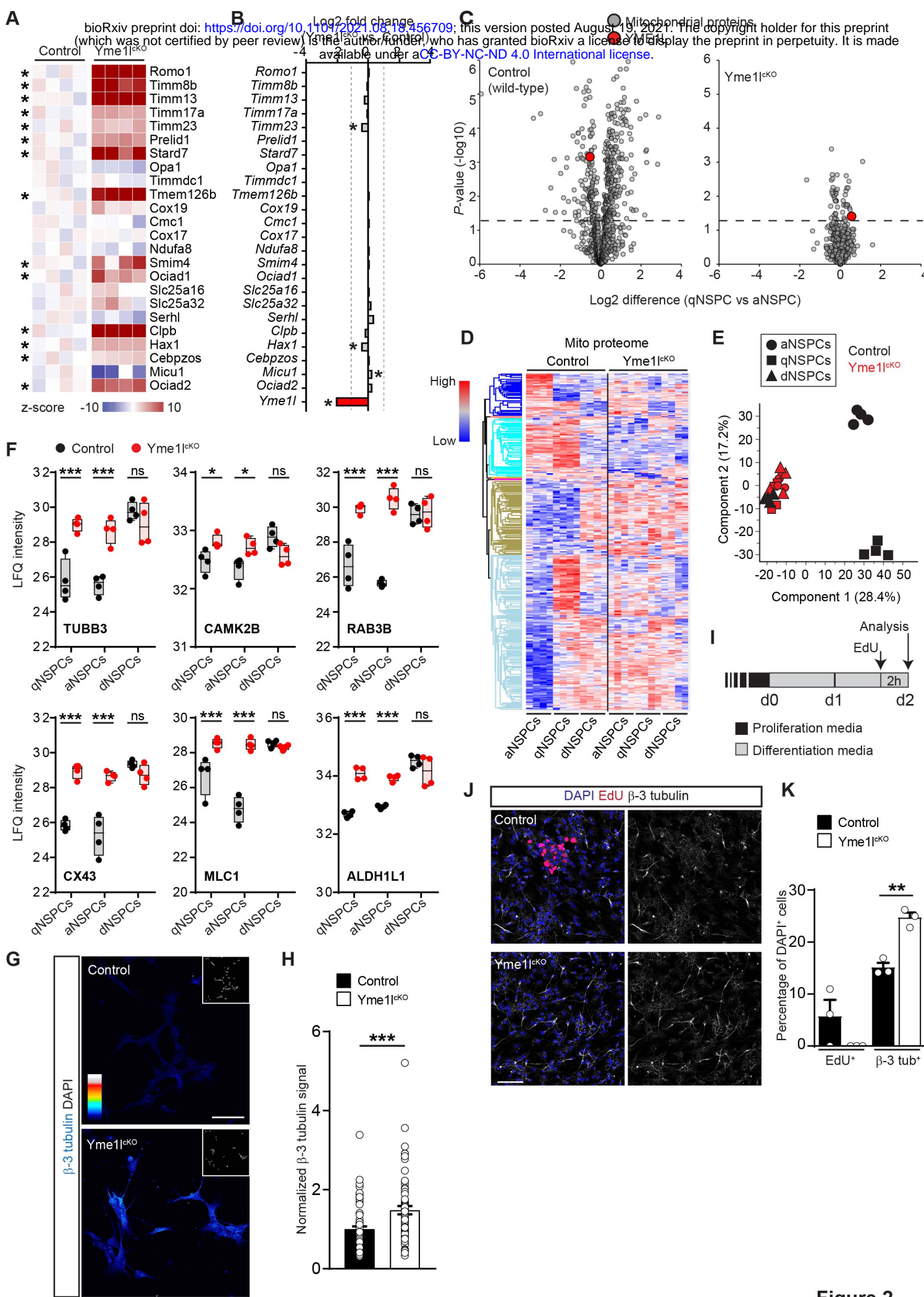


Figure 1



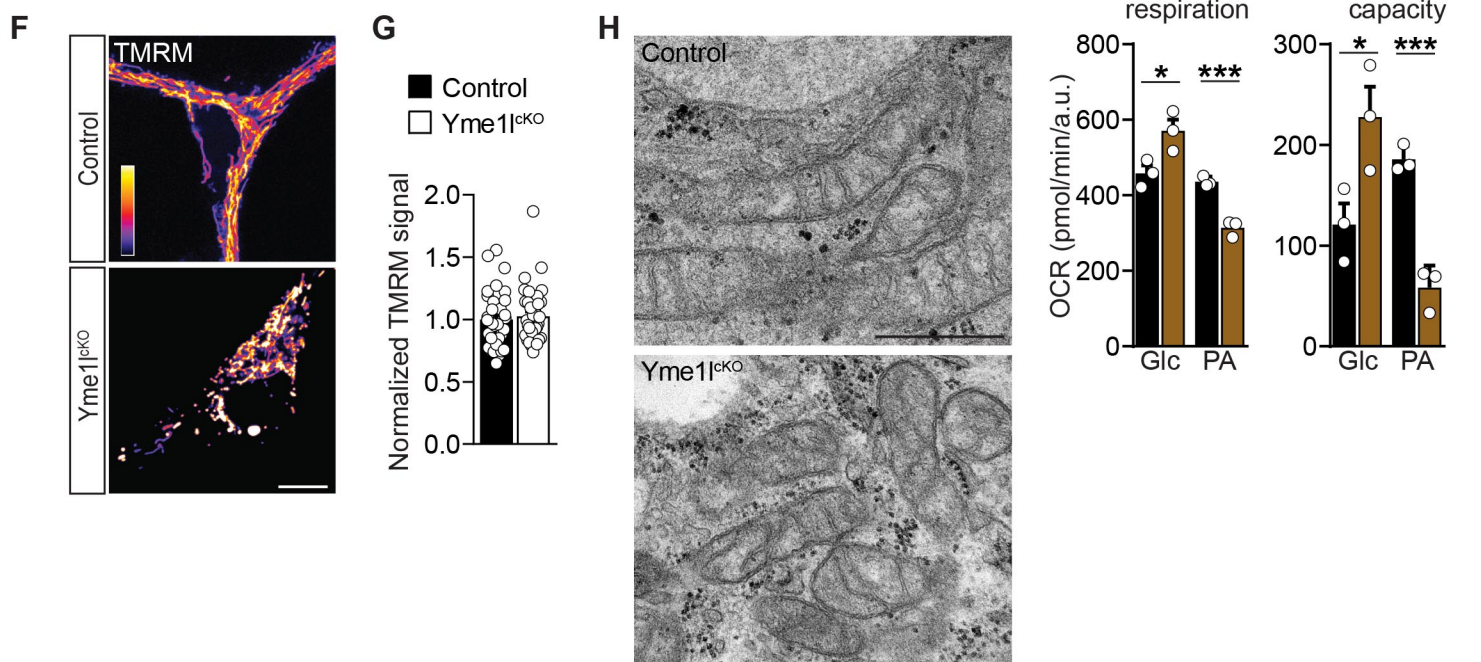
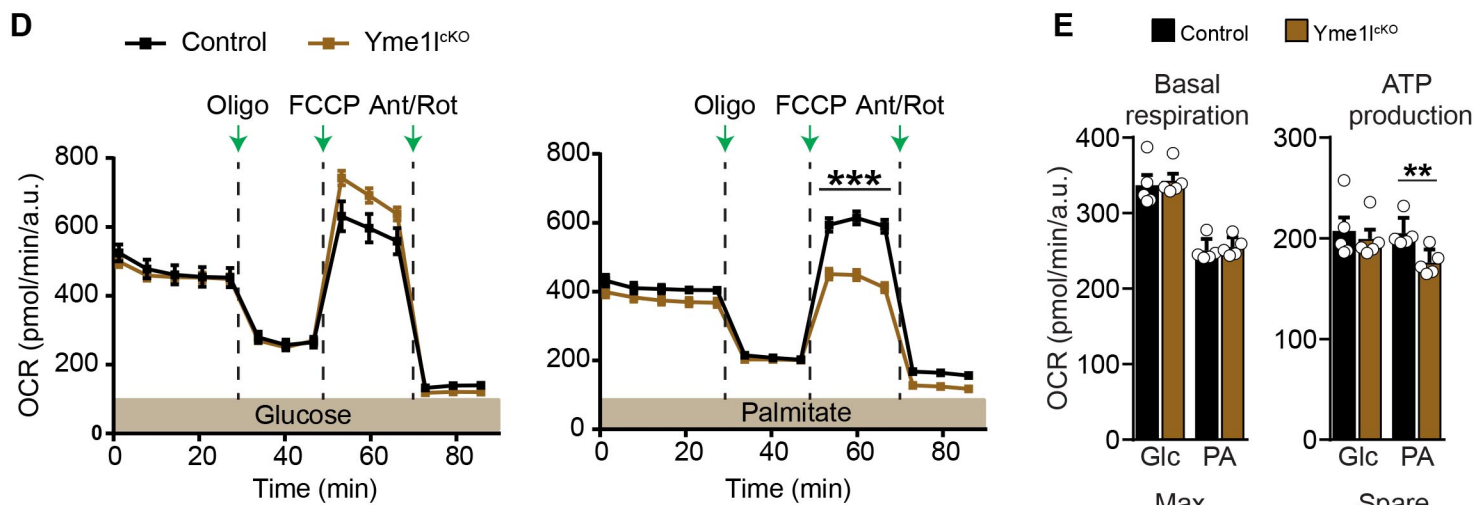
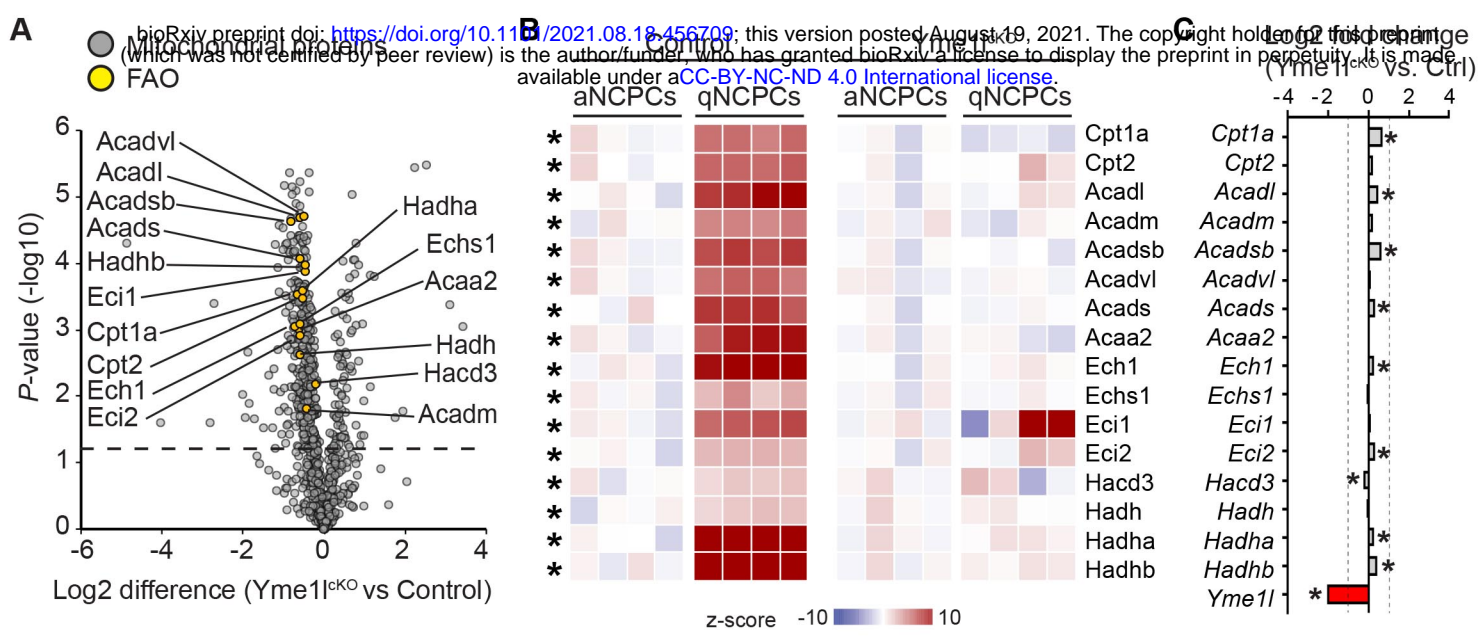


Figure 3

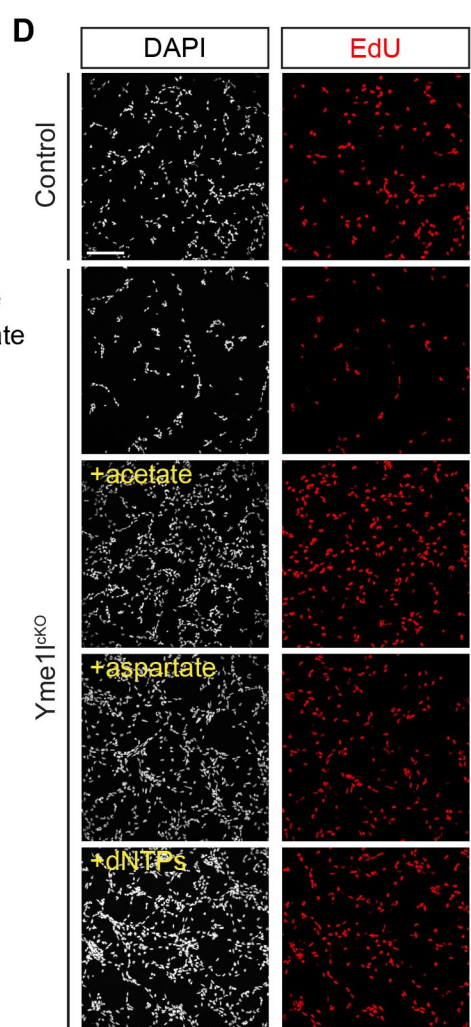
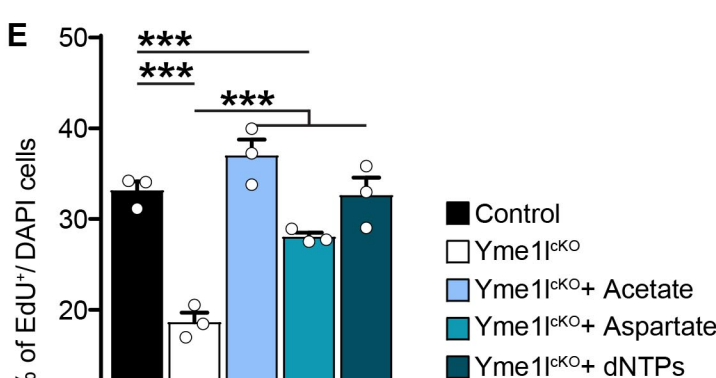
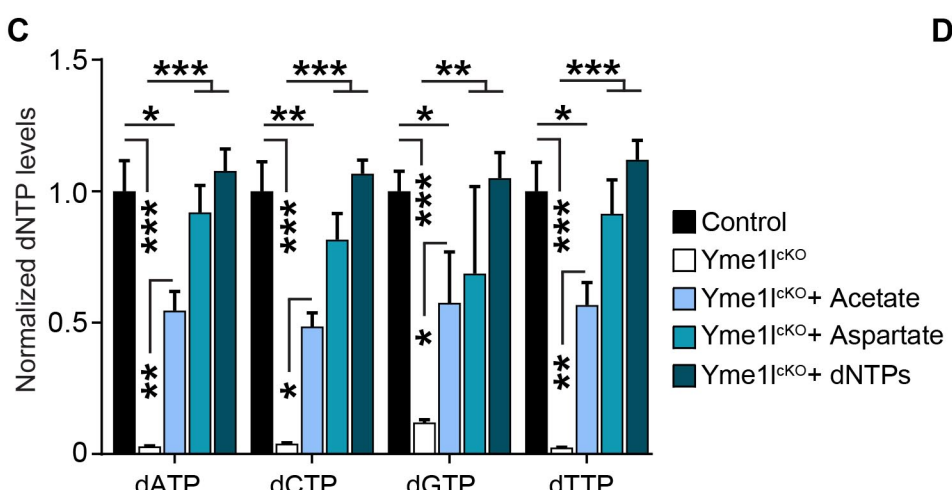
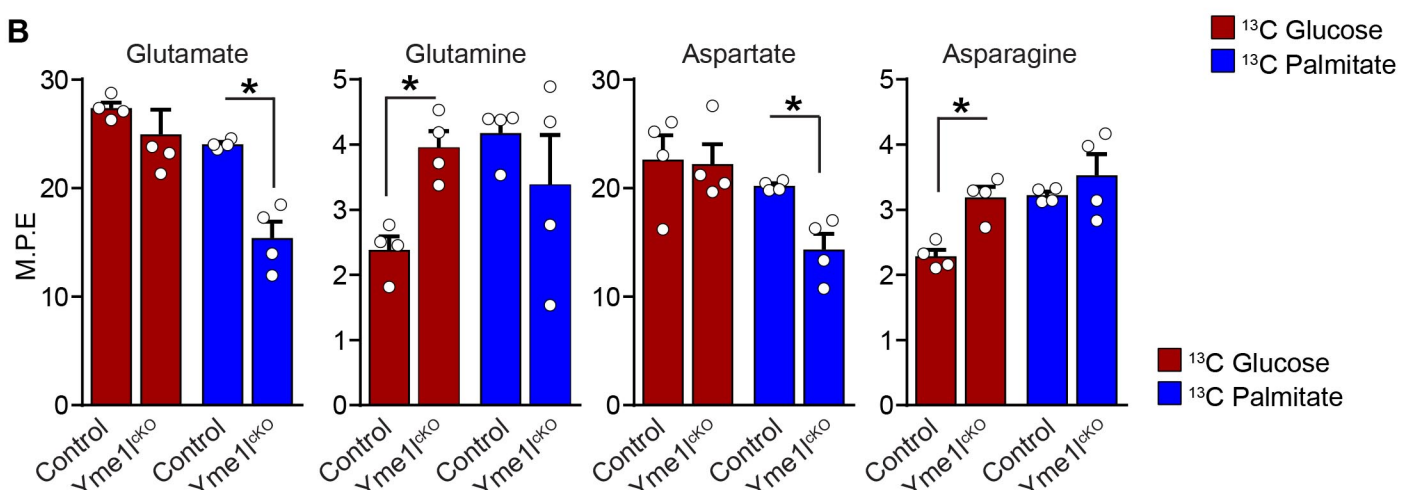
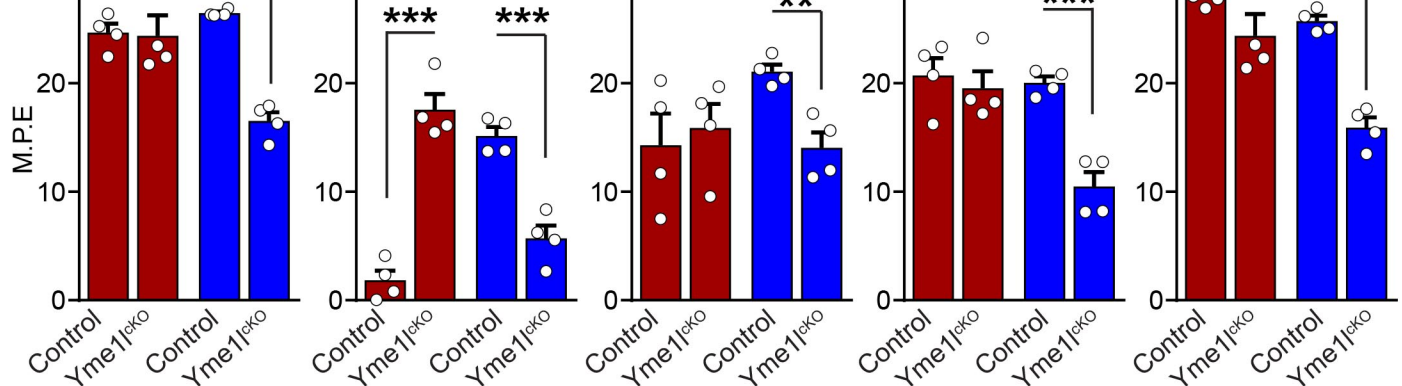


Figure 4

Yme1^{llox/lox}/Oma1^{llox/lox}
hGFAP::Cre^{ER} x mtYFP^{LSL}

-5 0 30 dpi

-5 0 5-6 10 dpi

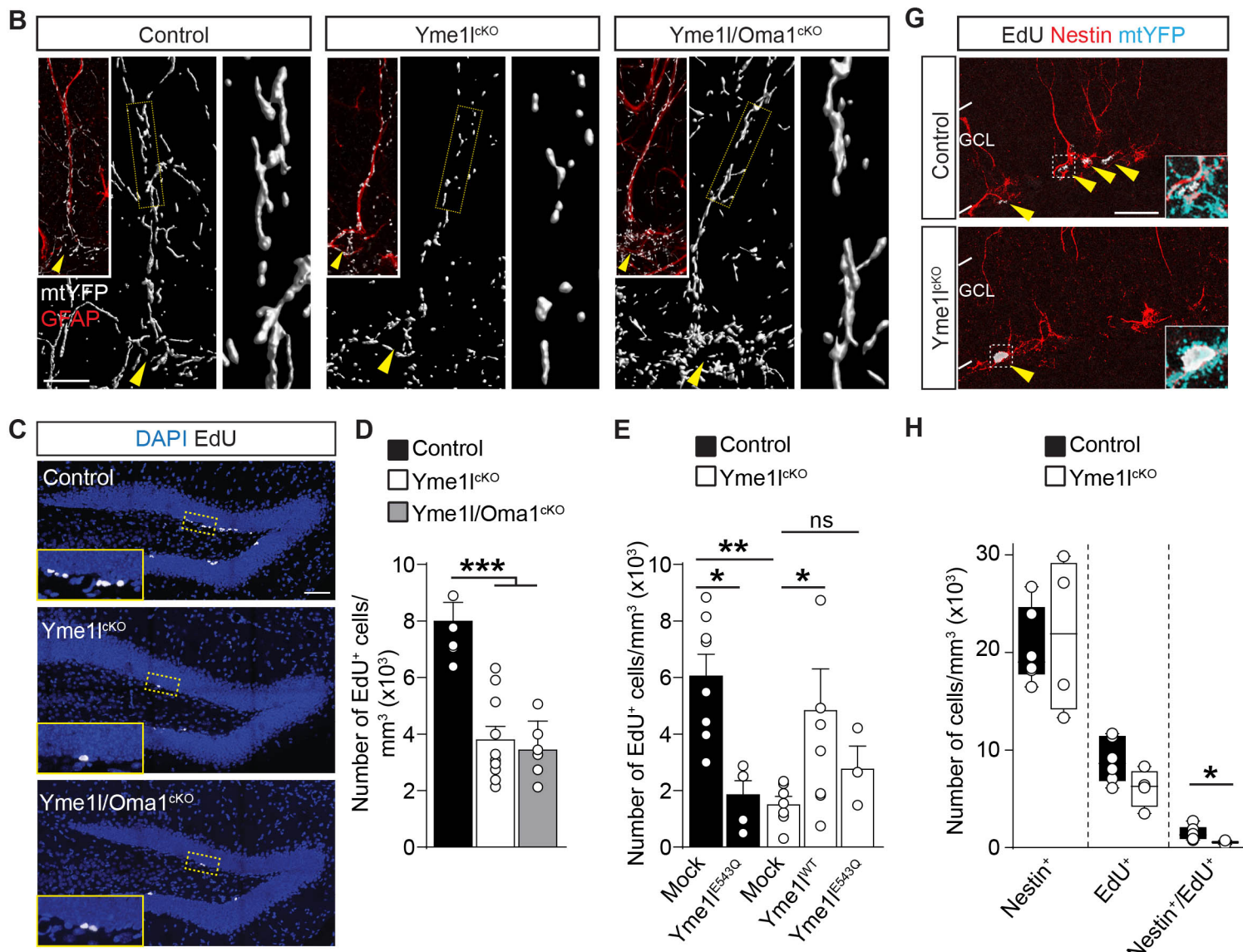


Figure 5

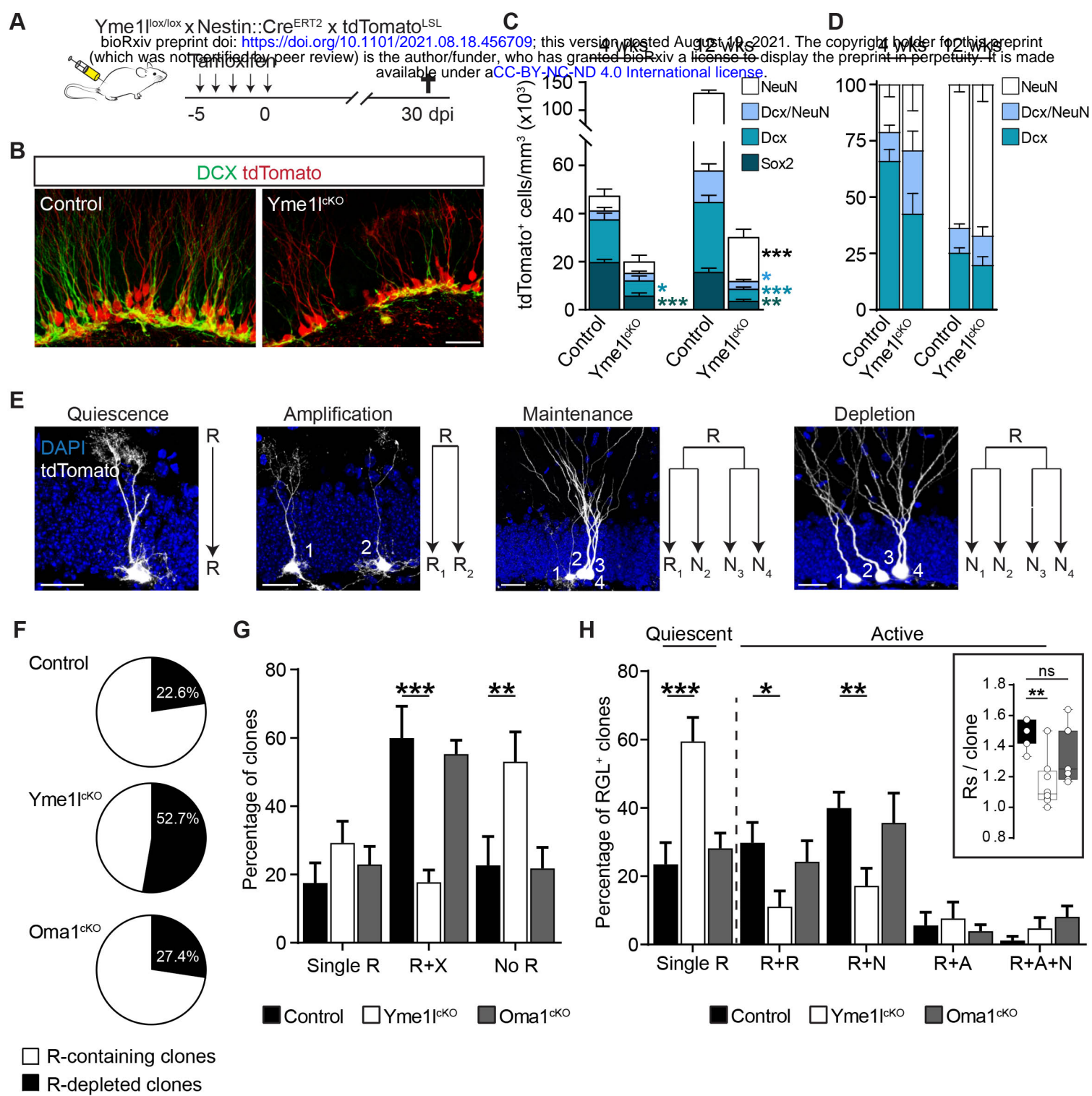


Figure 6

Legend to Supplemental Figures 1-6

Supplemental Figures 1-6

Legend to Supplemental Figures

Figure S1. Related to Figures 1 and 2. Assessment of NSPC state-dependent mitochondrial changes in proteome and metabolic fluxes. (A) PCA plot of aNSPCs, qNSPCs and ex-qNSPCs proteomic datasets. (B) Graph depicting the proteome-wide changes in protein expression levels of qNSPCs (in black) and ex-qNSPCs (in gray) with respect to aNSPCs, illustrating a wider distribution in the case of qNSPCs. (C) Heat maps of normalized LFQ intensities showing the differential expression of selected markers linked to proliferation (Mcm2, Mki67, PcnA, Nestin) as well as quiescence (Gfap, S100b, Slc1a2, Slc1a3) in aNSPCs and qNSPCs. Significant changes (n= 4 independent experiments per condition; FDR-adjusted ≤ 0.05) between qNSPCs and both aNSPCs and ex-NSPCs are indicated with a red asterisk. (D) Example of NSPC cultures isolated from the adult hippocampal DG and maintained either in active proliferation (Nestin+, left panel) or exposed to differentiation media for 14 days (following gradual withdrawal of growth factors), in which NSPCs acquire either stellate astrocytic (GFAP+) morphologies or a neuronal identity (Beta-3 tubulin+). Bar, 50 μ m. (E) Quantification of mitochondrial membrane potential (following incubation with 25 μ M TMRM) in aNSPCs and qNSPCs (n= 5 experiments; Welch's t-test). (F) Heat-maps of normalized LFQ intensities showing the differential expression (z-score) of electron transport chain (OXPHOS) subunits for complexes I-V in aNSPCs, qNSPCs and ex-qNSPCs. Significant changes (n= 4 independent experiments per condition; FDR-adjusted ≤ 0.05) are indicated with an asterisk (red asterisk: qNSPCs significant vs both aNSPCs and ex-NSPCs; black asterisk: qNSPCs significant vs only one other category). The right column reports on the fold change of mRNA levels of the corresponding genes between qNSPCs and aNSPCs (n= 4 independent experiments per condition; FDR-adjusted ≤ 0.05). (G-H) Heat-maps of normalized LFQ intensities showing the differential protein expression of FAO (G) and TCA cycle (H) enzymes in aNSPCs, qNSPCs and ex-qNSPCs. Significant changes (n= 4 independent experiments per condition; FDR-adjusted ≤ 0.05) are indicated with an asterisk (red asterisk: qNSPCs significant vs both aNSPCs and ex-NSPCs; black asterisk: qNSPCs significant vs only one other category). The right column reports on the fold change of mRNA levels of the corresponding genes between qNSPCs and aNSPCs (n= 4 independent experiments per condition; FDR-adjusted ≤ 0.05). (I) Graphs showing the mass isotopomer enrichment analysis for the indicated TCA cycle metabolites and amino acids in aNSPCs and qNSPCs (n= 3 independent experiments per condition; Holm-Sidak's t-test) after either $^{13}\text{C}_6$ -Glucose (in red) or $^{13}\text{C}_6$ -Palmitate (in blue) supplementation. M.P.E., Molar Percent Enrichment (calculated for each isotope). (J) Clustered heat-map showing the sample-to-sample distance relative to the RNA-Seq data obtained from aNSPCs and qNSPCs (n= 4 independent experiments per condition; FDR-adjusted ≤ 0.05). (K) Plots illustrating the extent of correlation (R^2) between protein and mRNA levels of the genes associated to FAO, TCA cycle, OXPHOS (Complexes subunits shown in E) and glycolysis (data obtained from n= 4 independent experiments per condition and dataset). Means \pm SEM; *, $P < 0.05$; **, $P < 0.01$; ***, $P < 0.005$.

Figure S2. Related to Figures 1, 2 and 3. Assessment of YME1L substrate specificity via Yme1l^{KO} NSPCs. (A) Heat-maps of normalized LFQ intensities of all detected mitochondrial proteases in NSPCs. Significant changes (n= 4 independent experiments; FDR-adjusted ≤ 0.05) are indicated with an asterisk (red asterisk: qNSPCs significant vs both aNSPCs and ex-NSPCs; black asterisk: qNSPCs significant vs only one other category). (B) Immunoblot of YME1L as well as of two of its validated proteolytic targets (TIMM17a and PRELID1) in qNSPCs and aNSPCs. OPA1 expression levels and SDHA loading controls are shown. (C) Experimental design illustrating the conditional deletion of *Yme1l* in adult NSPCs maintained *in vitro* via treatment with GFP-Cre or GFP-only AAVs. (D) Heat-maps of normalized LFQ intensities showing the differential expression of class II putative YME1L substrates. Significant changes (n= 4 independent experiments; FDR-adjusted ≤ 0.05) are indicated with an asterisk (red asterisk: qNSPCs significant vs both

bioRxiv preprint doi: <https://doi.org/10.1101/2021.08.18.456709>; this version posted August 19, 2021. The copyright holder for this preprint (which was not certified by peer review) is the author/funder, who has granted bioRxiv a license to display the preprint in perpetuity. It is made available under aCC-BY-NC-ND 4.0 International license.

(E) Fold change of mRNA levels of class II putative YME1L substrates between qNSPCs and aNSPCs (n= 4 independent experiments; FDR-adjusted ≤ 0.05). **(F)** Scatter plot showing class I putative YME1L substrates that underwent a significant accumulation in Yme11^{cKO} NSPCs. Substrates represented by a red dot indicate those that were also found at reduced protein levels in qNSPCs as compared to aNSPCs. **(G)** Heat maps of normalized LFQ intensities showing the differential expression of class II putative YME1L substrates in Yme11^{cKO} NSPCs. Asterisks indicate significant changes (n= 4 independent experiments; FDR-adjusted ≤ 0.05). **(H)** Immunoblots of NSPCs few days after treatment with the GFP-Cre AAV (Yme11^{cKO}) showing the ablation of YME1L as well as the accumulation of the YME1L substrate PRELID1 and the increased OMA1-mediated OPA1 processing leading to the expected accumulation of S-OPA1 isoforms c and e. **(I)** Quantification of YME1L and PRELID1 expression levels in Yme11^{cKO} NSPCs as shown in B (n= 4 independent experiments, Unpaired t-test). **(J)** Confocal pictures showing the morphology of mitochondria (immunolabeled against Tomm20) in control, Yme11^{cKO}, Oma1^{cKO} and Yme11/Oma1^{cKO} NSPCs. Bar, 10 μ m. **(K)** Examples of NSPCs belonging to the indicated genotypes and showing the extent of cell proliferation following 2h treatment with the base analog EdU (20 μ M). **(L)** Graph reporting on the quantification of NSPC proliferation as shown in E (n= 3-9 independent experiments, One-way Anova followed by Holm-Sidak's correction). **(M)** Volcano plots showing the changes in mitochondrial proteomes of Yme11^{cKO} and Oma1^{cKO} NSPCs compared to controls (n= 4 independent experiments per genotype). NSPC-specific class I YME1L substrates are highlighted in red. Cut-off line set at $-\log_{10}$ (P-value) = 1.3. Means \pm SEM; *, P < 0.05; **, P < 0.01; ***, P < 0.005.

Figure S3. Related to Figures 3 and 4. Metabolic analysis of Yme11^{cKO} NSPCs. **(A)** Volcano plot showing the changes in the mitochondrial proteome of Oma1^{cKO} NSPCs compared to controls (n= 4 independent experiments per genotype). FAO enzymes are highlighted in yellow. Cut-off line set at $-\log_{10}$ (P-value) = 1.3. **(B)** Volcano plots showing the changes in the mitochondrial proteome of Mfn1^{cKO} and Mfn2^{cKO} NSPCs compared to controls (n= 3 independent experiments per genotype). FAO enzymes are highlighted in yellow. Cut-off line set at $-\log_{10}$ (P-value) = 1.3. **(C)** Representative pictures of NSPCs obtained from control, Mfn1^{cKO} and Mfn2^{cKO} immunostained for the mitochondrial marker TOMM20. Bar, 10 μ m. **(D)** Proliferation assay in control, Mfn1^{cKO} and Mfn2^{cKO} NSPCs (n= 3-6 independent experiments per genotype). **(E)** Measurement of NAD/NADH ratio in control and Yme11^{cKO} NSPCs (n= 3 independent experiments). **(F)** Graphs showing the mass isotopomer enrichment analysis for the indicated metabolites in control and Yme11^{cKO} NSPCs (n= 4 independent experiments per condition; Holm-Sidak's t-test) after either ¹³C₆-Glucose (in red) or ¹³C₆-Palmitate (in blue) supplementation. M.P.E., Molar Percent Enrichment (calculated for each isotope). **(G)** Extracellular acidification rate (ECAR) measurement in control and Yme11^{cKO} NSPCs fed with glucose (n= 30 repetitions, 3 independent experiments; Holm-Sidak multiple t-test). **(H)** Measurement of glycolytic metabolites in Yme11^{cKO} NSPCs, normalized to control NSPCs (4 independent experiments; Holm-Sidak multiple t-test). **(I)** Measurement of TCA cycle metabolites in Yme11^{cKO} NSPCs, normalized to control NSPCs (4 independent experiments; Holm-Sidak multiple t-test). **(J)** Transcriptomic analysis in NSPCs of interferon-stimulated genes previously described for being induced in Yme11^{cKO} MEFs (4 independent experiments; FDR-adjusted ≤ 0.05). Means \pm SEM; *, P < 0.05; **, P < 0.01; ***, P < 0.005.

Figure S4. Related to Figure 5. Lack of YME1L impairs NSPC proliferation in the adult DG and SVZ. **(A)** Section of the DG of an hGFAP::Cre^{ER} x mtYFP^{LSL} mouse after tamoxifen administration, showing the extent of recombination (on the basis of the mtYFP reporter gene expression) in GFAP+ cells lining the SGZ (arrowheads). Bar,

bioRxiv preprint doi: <https://doi.org/10.1101/2021.08.18.456709>; this version posted August 19, 2021. The copyright holder for this preprint (which was not certified by peer review) is the author/funder, who has granted bioRxiv a license to display the preprint in perpetuity. It is made available under aCC-BY-NC-ND 4.0 International license.

(B) Experimental design illustrating the tamoxifen-induced conditional deletion of *Oma1* in hGFAP::Cre^{ER} x mtYFP^{LSL} mice. **(C)** Examples EdU labelling in the DG of the indicated genotypes. Bar, 70 μ m. **(D)** Quantification of NSPC proliferation for the indicated genotypes (n= 5 mice per group; Unpaired t-test). **(E)** Examples EdU labelling in the SVZ lining the lateral ventricle of the indicated genotypes. Insets show an overview of the lateral ventricle. Bar, 50 μ m. **(F)** Quantification of NSPC proliferation in the SVZ for the indicated genotypes (n= 3-6 mice per group; One-way Anova followed by Holm-Sidak's multiple comparison test). **(G)** Examples showing the DG of the indicated genotypes and the density of Sox2⁺ cells (identifying both radial glia-like NSPCs and astrocytes) as well as that of Ki67⁺ (proliferating) cells. Insets show enlargements of the boxed areas. Arrowheads point to double positive (Sox2⁺/ki67⁺) cells. Bar, 100 μ m. **(H)** Quantification of Sox2⁺ cells (including both radial glia-like NSPCs and astrocytes) in the SGZ of the DG of the indicated genotypes (n= 3-4 mice per group, One-way Anova followed by Holm-Sidak's multiple comparison test). **(I)** Quantification of dividing Sox2⁺/ki67⁺ cells in the SGZ of the DG of the indicated genotypes (n= 3-4 mice per group, One-way Anova followed by Holm-Sidak's multiple comparison test). Means \pm SEM; *, P < 0.05; **, P < 0.01.

Figure S5. Related to Figure 5. Regulation of NSPC proliferation by YME1L is independent from changes in mitochondrial dynamics. **(A)** Quantification of control or Yme11^{cKO} NSPCs proliferation *in vitro* following transduction with the indicated AAVs and treatment with EdU (n= 3 independent experiments; one-way Anova followed by Holm-Sidak's multiple comparison test). **(B)** Experimental design illustrating the tamoxifen-induced conditional deletion of *Yme11* in hGFAP::Cre^{ER} x mtYFP^{LSL} mice followed by stereotactic delivery of AAVs encoding for Yme11^{WT} or the proteolytically inactive variant Yme11^{E543Q}. EdU treatments were performed briefly before sacrifice to assess changes in NSPC proliferation. **(C)** Examples of EdU-treated animals for the indicated genotypes and conditions to assess NSPC proliferation in the DG. Bar, 40 μ m. **(D)** Examples of individual radial glia-like mtYFP⁺/GFAP⁺ NSPCs in the DG of the indicated genotypes and following injection of mock, Yme11^{WT} or Yme11^{E543Q}-encoding AAVs, showing the corresponding changes in mitochondrial morphology. Arrowheads points to the cell soma. Right panels show zooms of the boxed areas in the cell soma and along the main radial process. Bar, 15 μ m. **(E)** Experimental design illustrating the tamoxifen-induced conditional deletion of *Yme11* in hGFAP::Cre^{ER} x mtYFP^{LSL} mice followed by EdU treatments (which incorporates into dividing cells) 4 days before sacrifice and assessment of still-dividing EdU⁺ cells by immunostaining against the proliferation marker Ki67. **(F)** Examples of EdU-treated animals as depicted in E for the indicated genotypes showing proliferating EdU⁺/Ki67⁺ cells in the DG. Low panels show enlargements of the boxed areas and report on individual and merged channels. Arrowheads point to double positive (EdU⁺/Ki67⁺) cells in the SGZ. Bar, 100 μ m. **(G)** Quantification of total EdU⁺ and EdU⁺/Ki67⁺ cells in the SGZ of control and Yme11^{cKO} mice (n= 10-12 mice, two-way Anova). **(H)** Proportion of EdU⁺/Ki67⁺ cells of all EdU⁺ cells (n= 10-12; unpaired t-test). Means \pm SEM; *, P < 0.05; **, P < 0.01; ***, P < 0.005.

Figure S6. Related to Figure 6. Analysis of type II NSPCs and clonal analysis in Yme11^{cKO} NSPC. **(A)** Examples of Tbr2 immunostaining in the DG of Yme11^{lox/lox} x Nestin::Cre^{ERT2} x tdTomato^{LSL} and control mice. Insets report zooms of the boxed areas. Bar, 20 μ m. **(B)** Quantification of TdTomato⁺ and Tbr2⁺ cells in Yme11^{cKO} mice (n= 6 mice per group, unpaired t-test). **(C)** Example of a single recombined TdTomato⁺ radial glia-like NSPC following a single low dose tamoxifen administration. The low panel shows an enlargement of the boxed area. Bars, 80 and 25 μ m. **(D)** Tamoxifen dose-dependent increase in the number of TdTomato⁺ cells found in the whole DG of Nestin::Cre^{ERT2} x

TdTomato^{LSL} mice by 1 week after injection. (E) Quantification of clone size per genotype (n= 7-9 mice per genotype).

Means \pm SEM; *, $P < 0.05$.

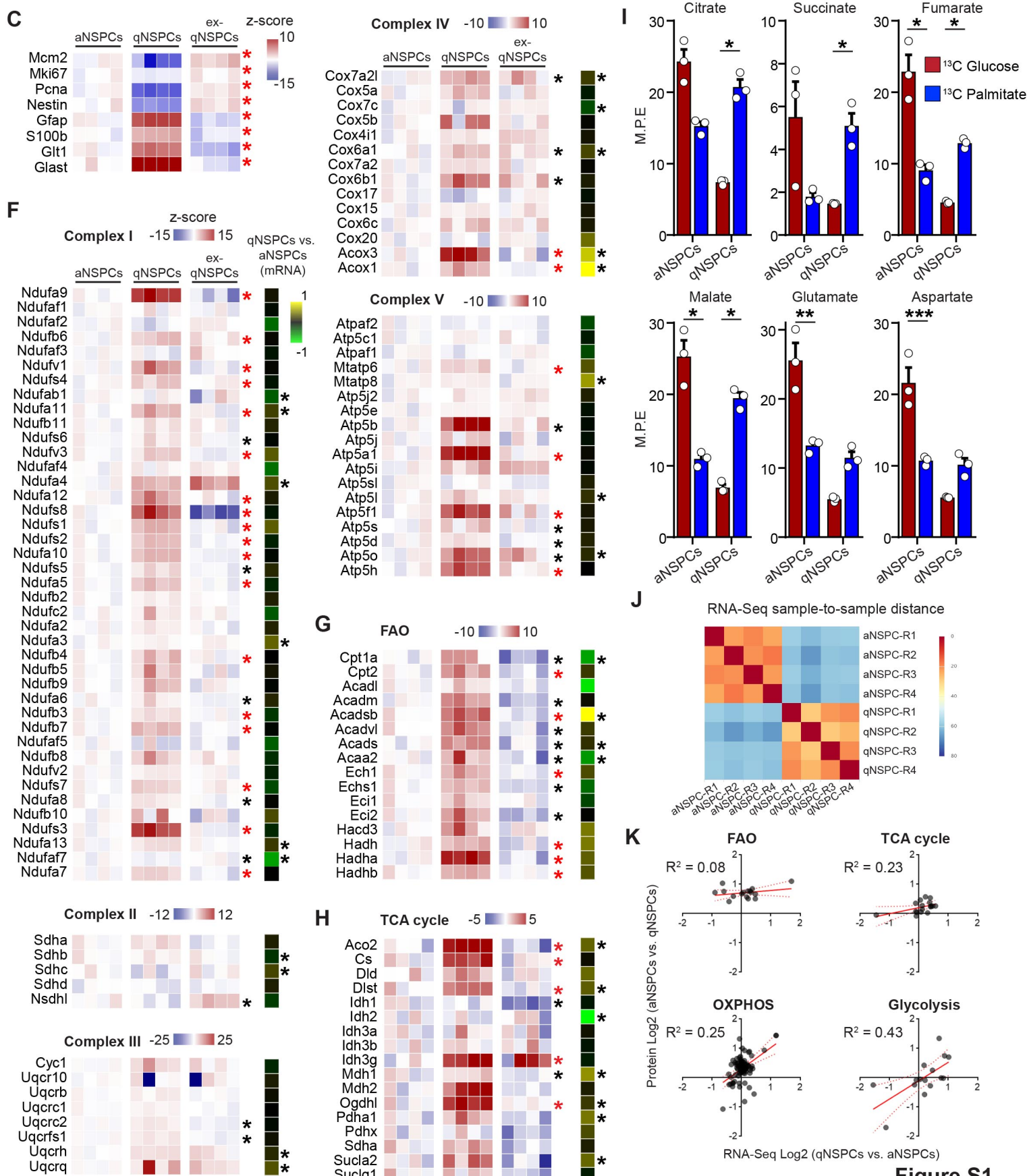
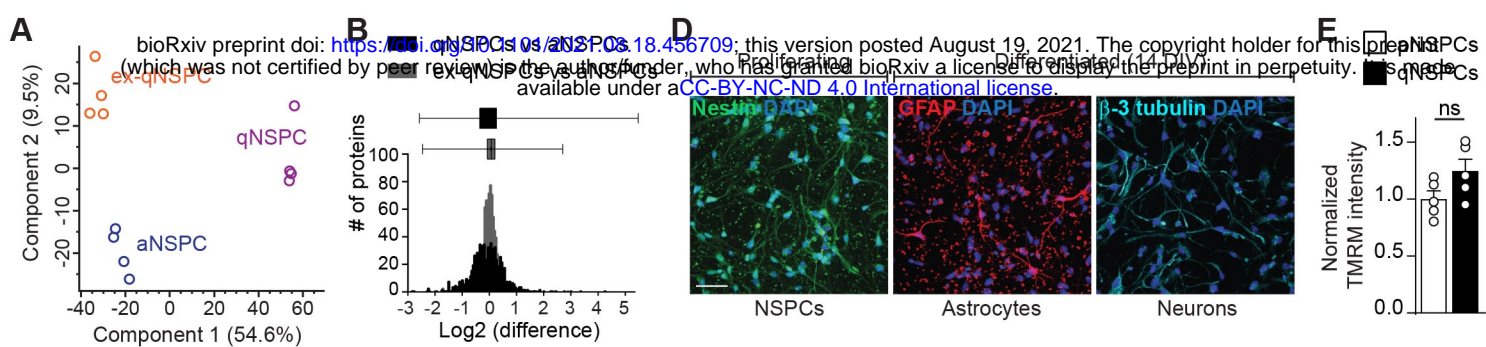
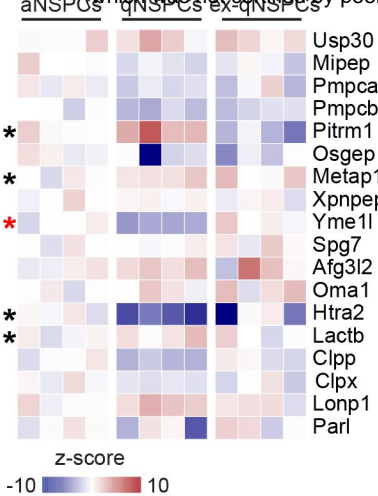
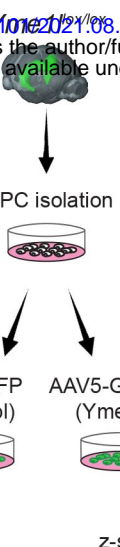
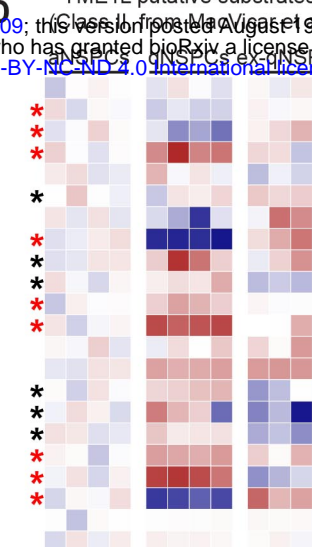
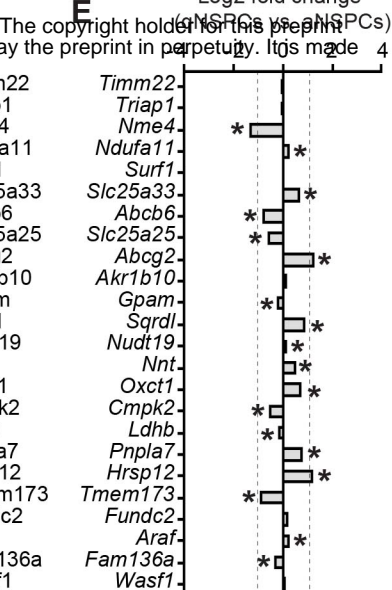
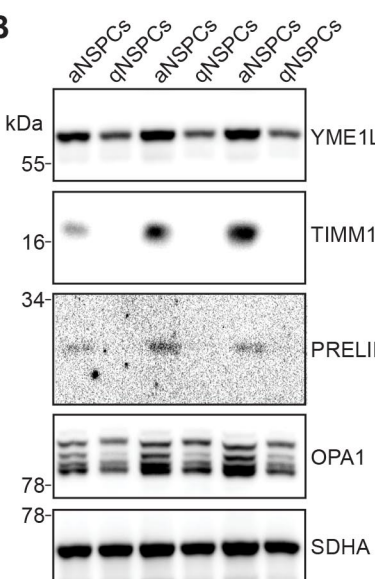
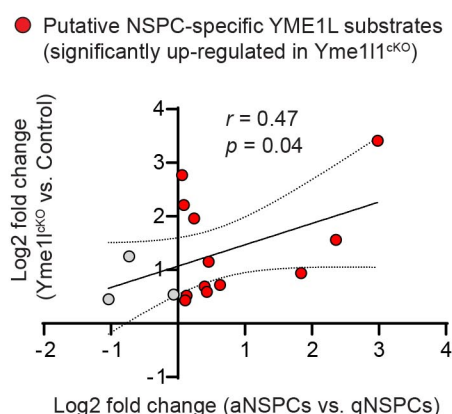
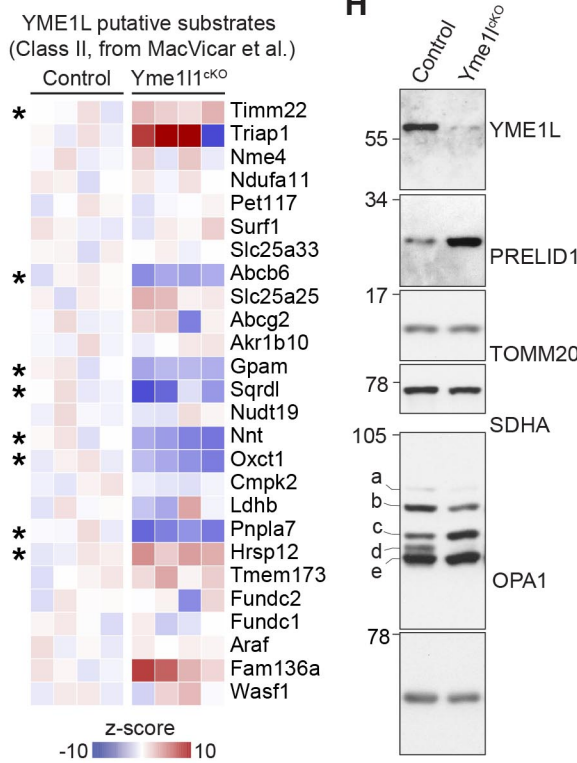
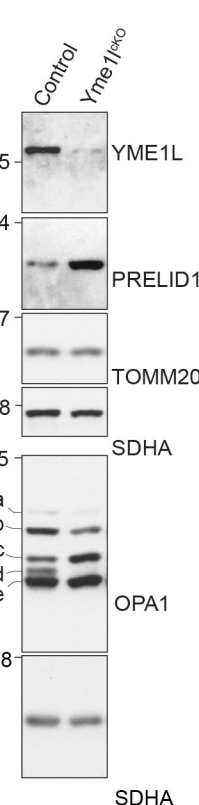
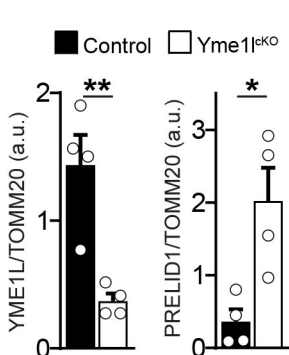
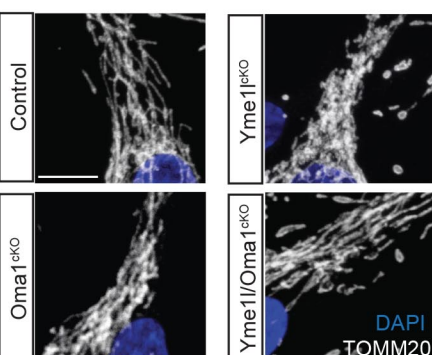
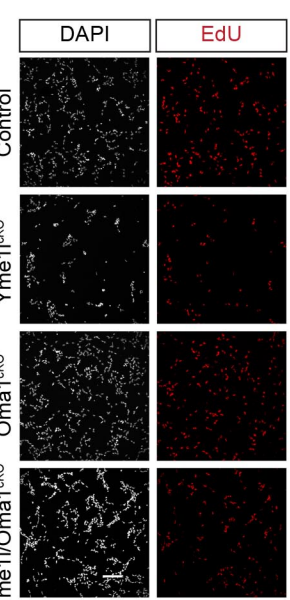
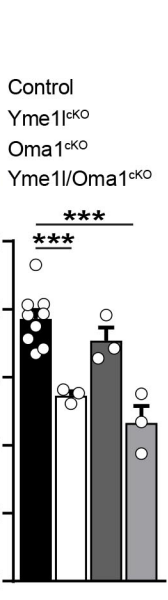
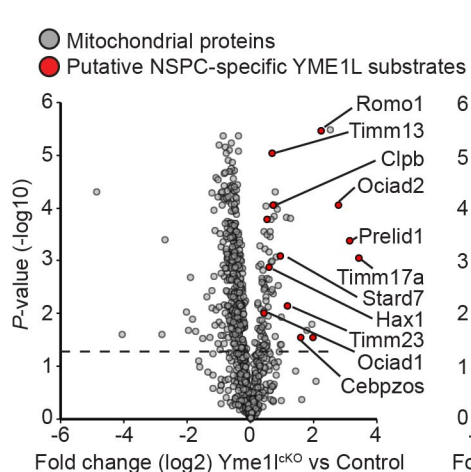


Figure S1

A

Mitochondrial bioRxiv preprint doi: <https://doi.org/10.1101/2021.08.18.456709>; this version posted August 19, 2021. The copyright holder for this preprint (which was not certified by peer review) is the author/funder, who has granted bioRxiv a license to display the preprint in perpetuity. It is made available under aCC-BY-NC-ND 4.0 International license.

**C****D****E****B****F****G****H****I****J****K****L****M**

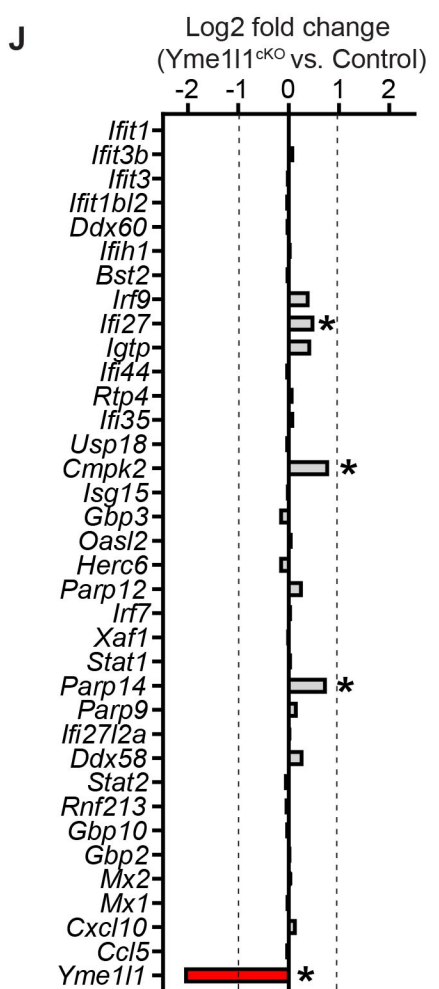
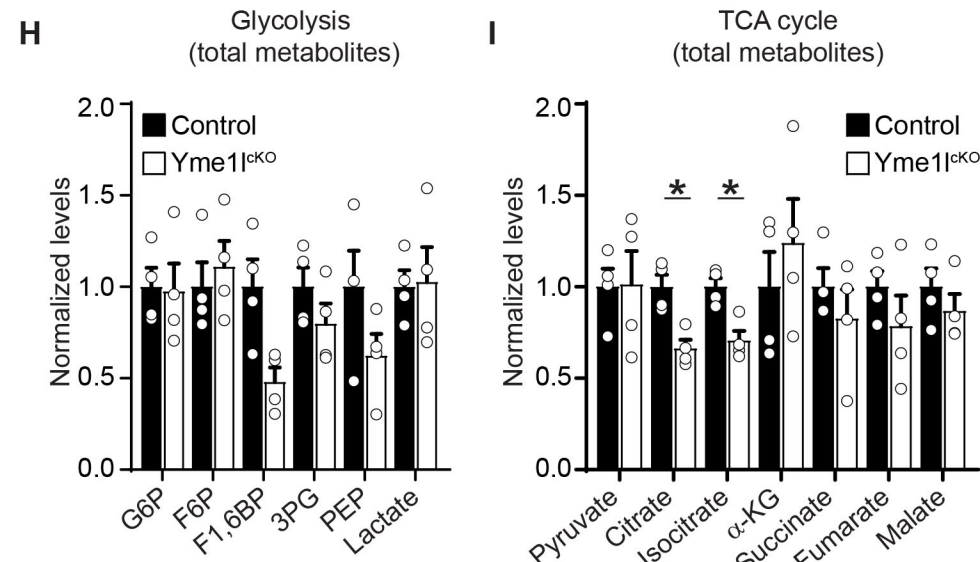
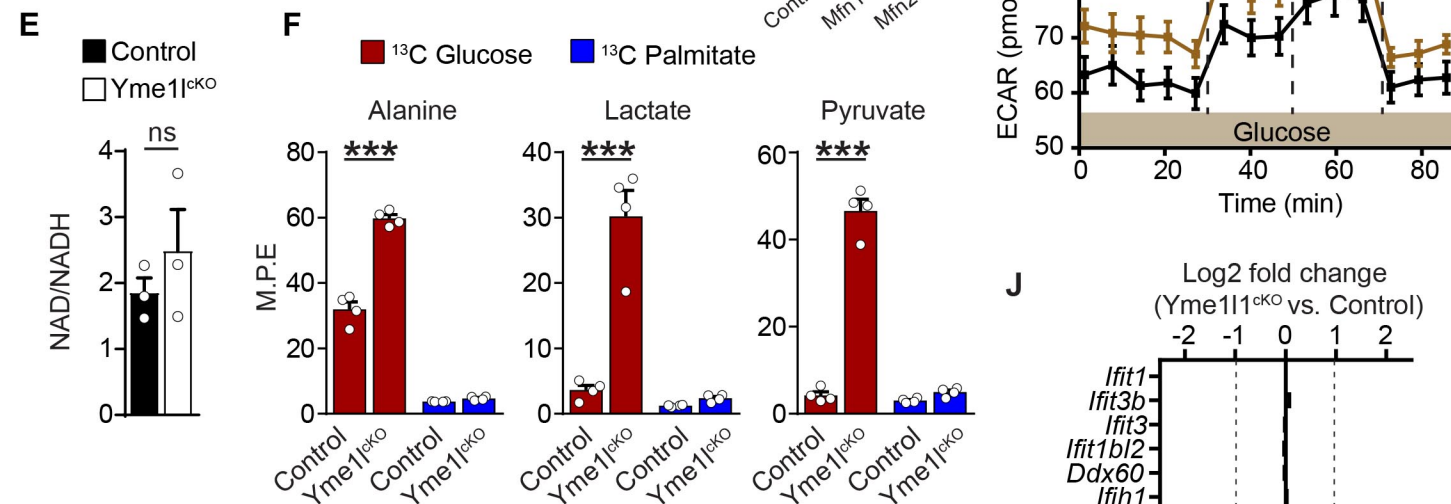
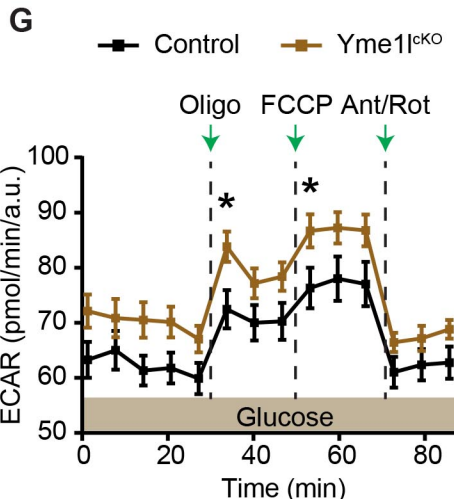
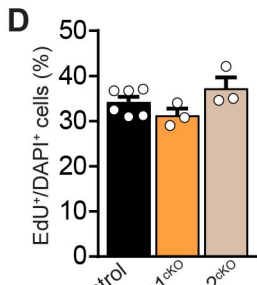
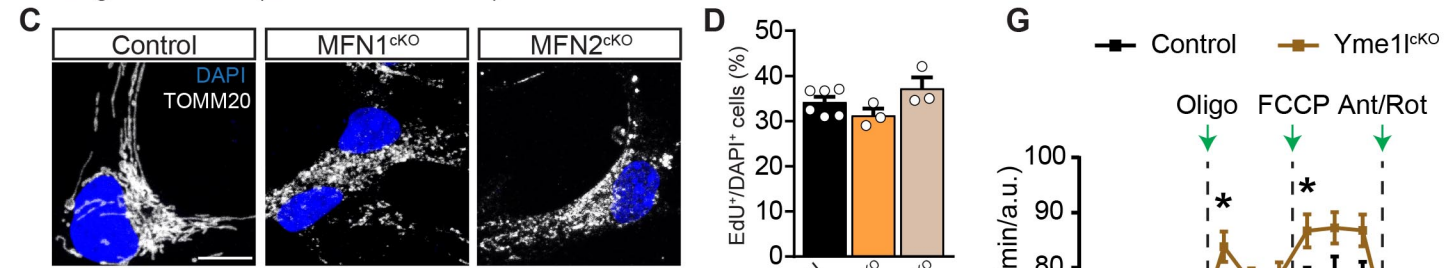
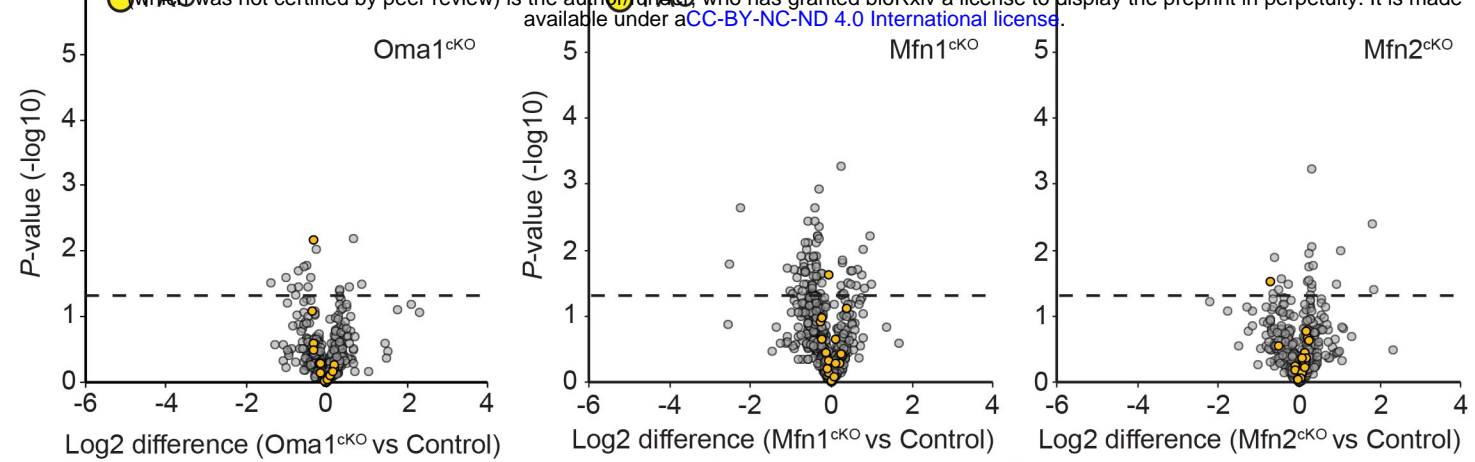
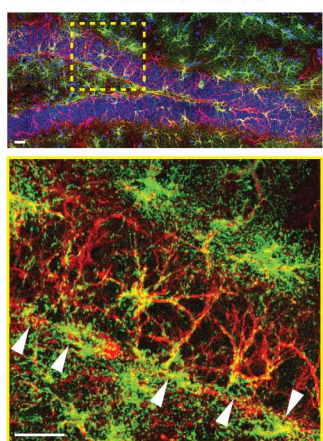


Figure S3

A**B**

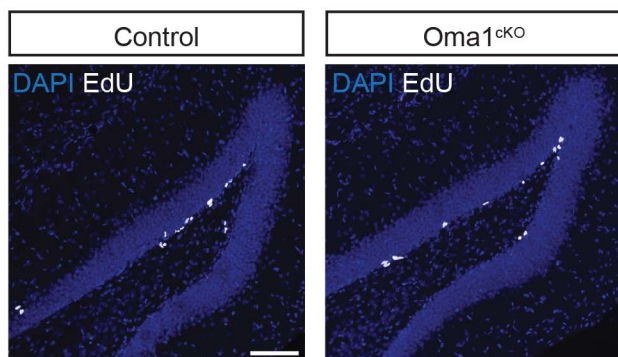
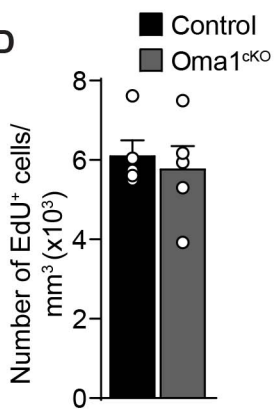
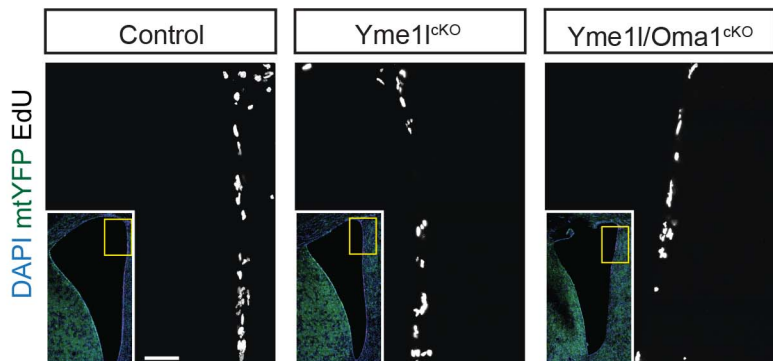
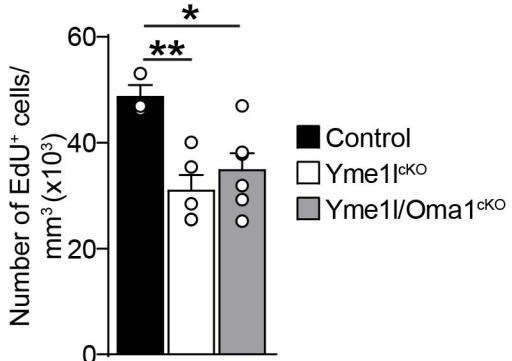
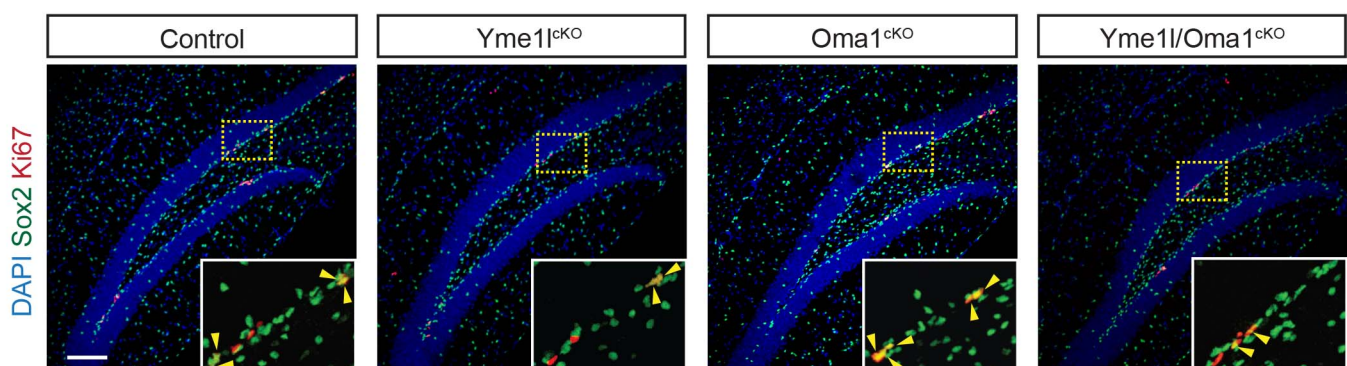
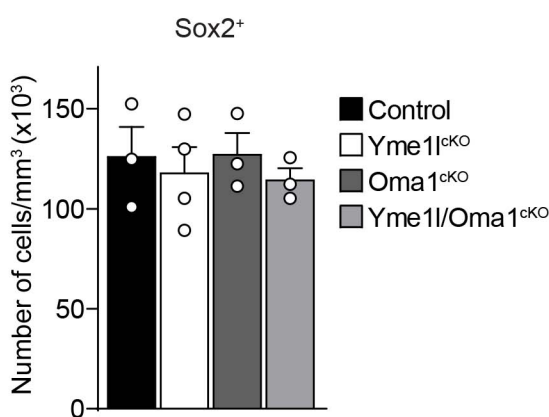
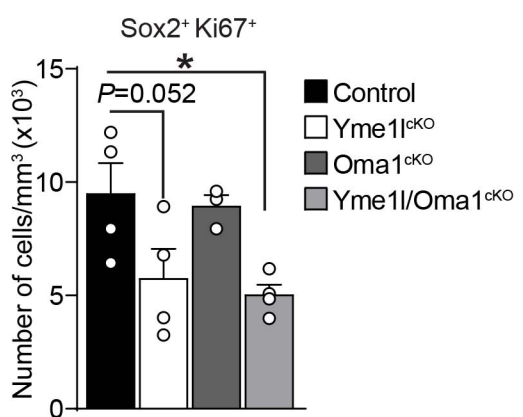
bioRxiv preprint doi: <https://doi.org/10.1101/2021.08.18.456709>; this version posted August 19, 2021. The copyright holder for this preprint (which was not certified by peer review) is the author/funder, who has granted bioRxiv a license to display the preprint in perpetuity. It is made available under aCC-BY-NC-ND 4.0 International license.

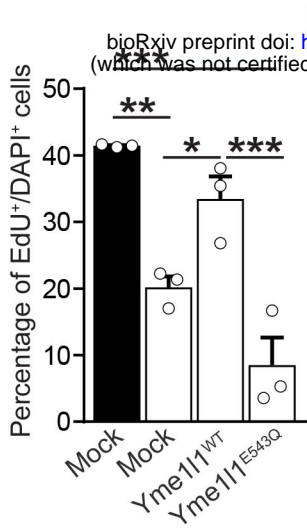
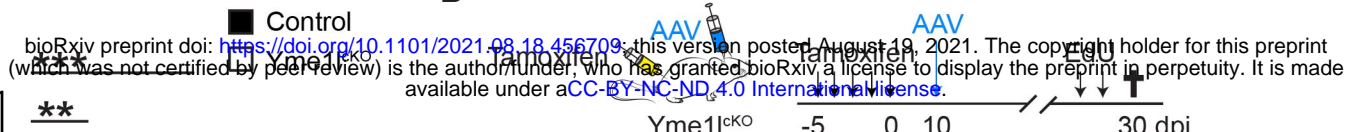
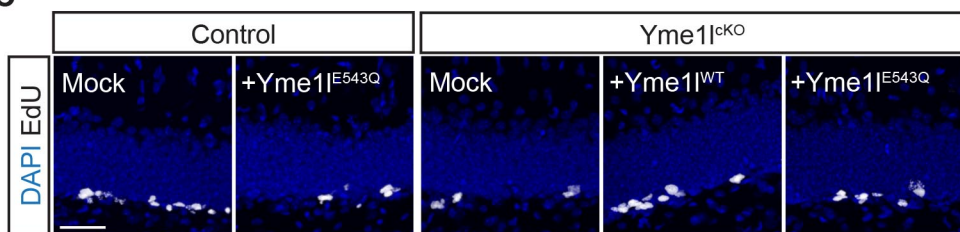
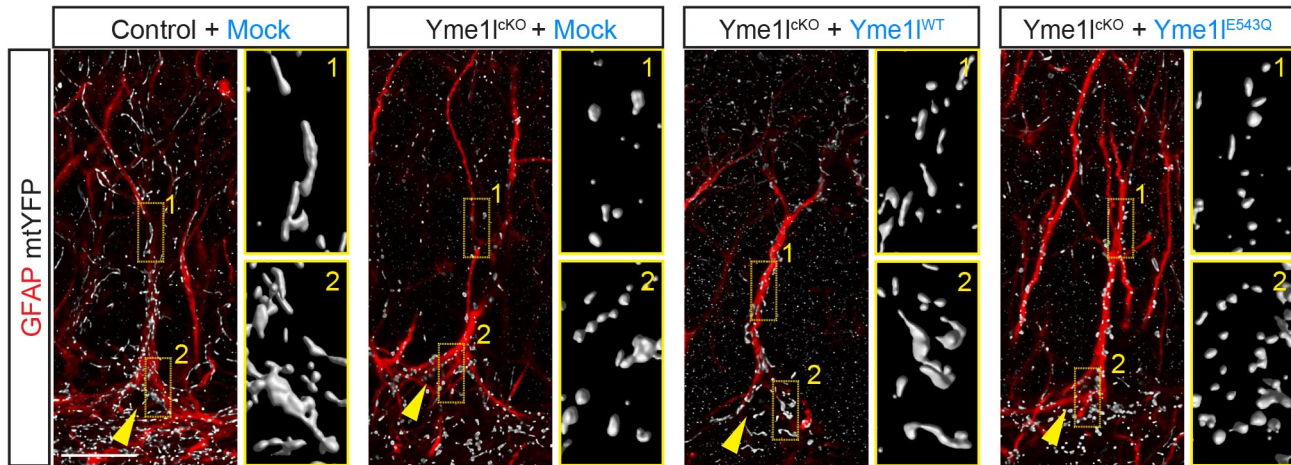
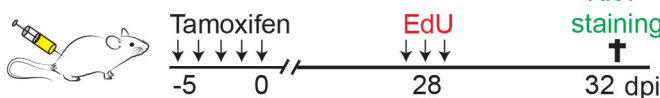
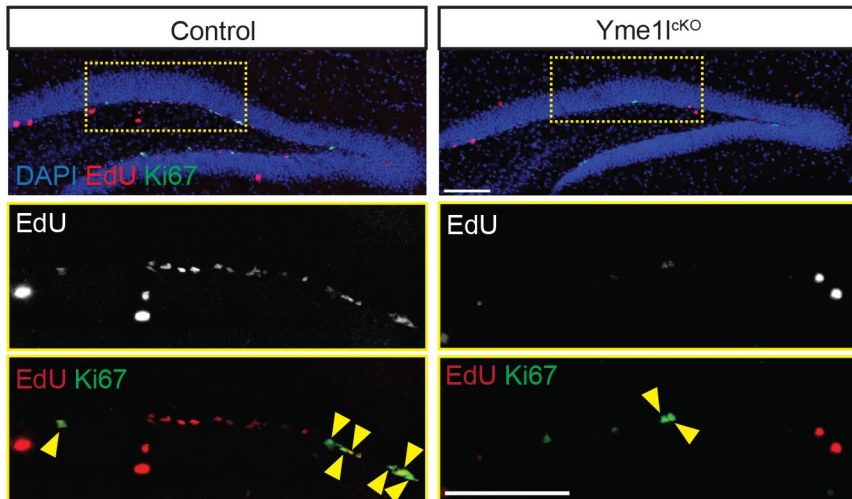
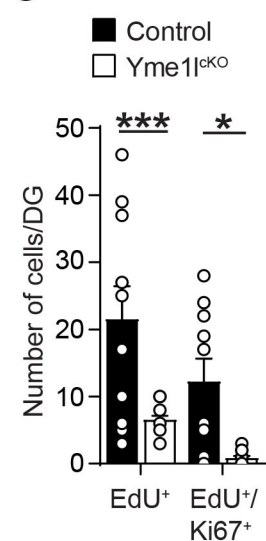
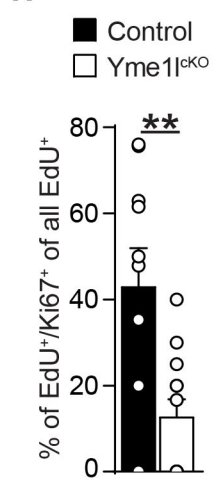
Tamoxifen

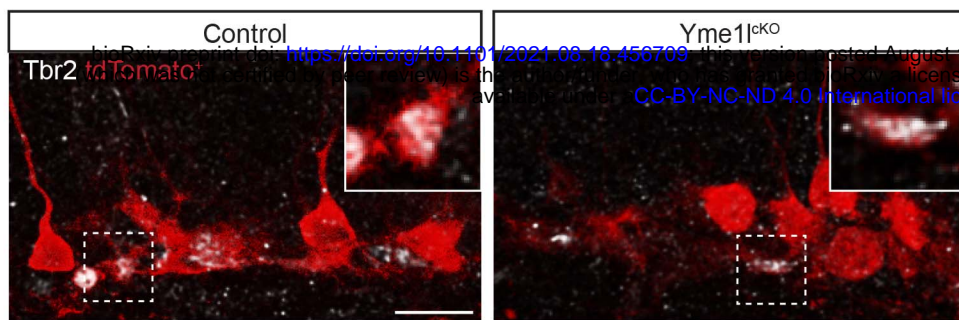
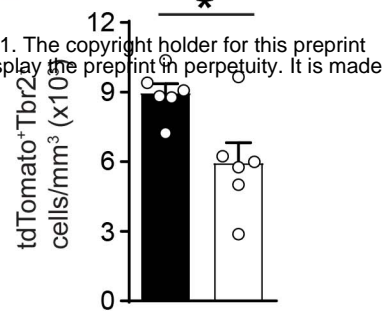
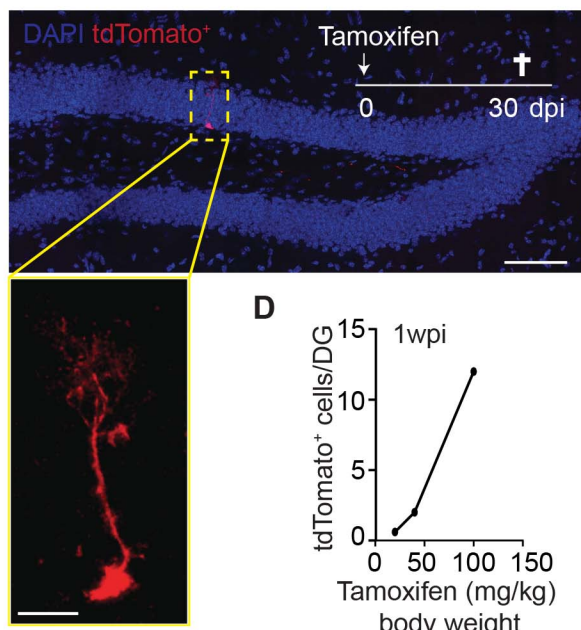
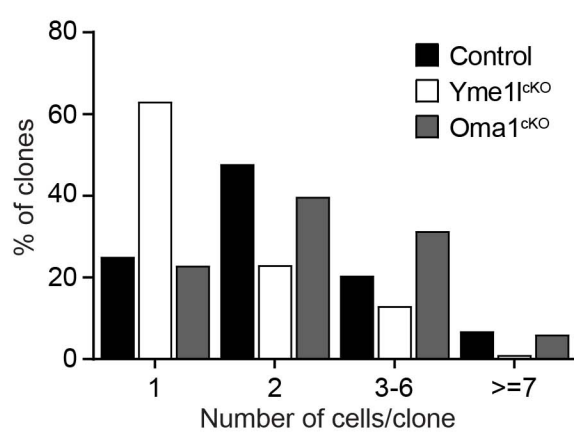
Oma1^{lox/lox} x hGFAP::Cre^{ER} x mtYFP^{LSL}

EdU

30 dpi

C**D****E****F****G****H****I**

A**B****C****D****E****F****G****H**

A**B****C****E****D**